



Cao, Z., White, C. and Kontis, K. (2021) Numerical investigation of rarefied vortex loop formation due to shock wave diffraction with the use of vorticity. *Physics of Fluids*, 33(6), 067112. (doi: [10.1063/5.0054289](https://doi.org/10.1063/5.0054289)).

This is the author's final accepted version.

There may be differences between this version and the published version. You are advised to consult the publisher's version if you wish to cite from it.

<http://eprints.gla.ac.uk/241432/>

Deposited on: 12 May 2021

Enlighten – Research publications by members of the University of Glasgow
<http://eprints.gla.ac.uk>

Numerical investigation of rarefied vortex loop formation due to shock wave diffraction with the use of rorticity

Ziqu Cao (曹子曲)^{1, a)} Craig White,^{1, b)} and Konstantinos Kontis^{1, c)}
*James Watt School of Engineering, University of Glasgow, Glasgow G12 8QQ,
UK*

(Dated: May 9, 2021)

When compressed gas is ejected from a nozzle into a low-pressure environment, the shock wave diffracts around the nozzle lip and a vortex loop will form. The phenomenon has been widely investigated in the continuum flow regime, but how the shock diffraction and vortex behave under rarefied flow conditions has not received as much attention. It is necessary to understand this transient flow in rarefied environments to improve thrust vector control and avoid potential contamination and erosion of spacecraft surfaces. This work provides numerical results of the vortex loop formation caused by shock wave diffraction around a 90° corner using the direct simulation Monte Carlo method and the compressible Navier-Stokes equations with the appropriate Maxwell velocity slip and the von Smoluchowski temperature jump boundary conditions. The Mach number and rarefaction effects on the formation and evolution of the vortex loop are discussed. A study of the transient structures of vortex loops has been performed using the rorticity concept. A relationship of mutual transformation between the rorticity and shear vectors has been discovered, demonstrating that the application of this concept is useful to understand vortex flow phenomena.

Keywords: rarefied; DSMC; vortex loop; shock diffraction; rorticity

I. INTRODUCTION

A. Background

In the past two decades, many micro-satellites, e.g., CubeSats, have been sent into space for purposes such as earth observation, telecommunication, and navigation³³. The continuous growth of applications for cost-effective micro-satellites in low Earth orbit (LEO) is leading to a requirement for specialized thruster systems that can provide thrusts in the micro- and mili-Newton range, in order to control their motions and orbits⁸. Micro-propulsion systems can be classed as electric and non-electric types⁴⁸. The hardware of electric propulsion systems, such as pulsed plasma thrusters, is more complicated than that of the non-electric type, which includes cold gas, liquid, and solid rocket propulsion systems⁴⁸. The technologies used in electric propulsion systems must be validated to be reliable before extensive practical usage. Non-electric propulsion systems (e.g. cold gas micro-thrusters) have been deployed extensively for orbit transfer and manoeuvring due to their high reliability³³. A common point shared by both of these propulsion technologies is that they operate by ejecting a mass of gas from a nozzle at high velocity to produce thrust.

During the transient period as a thruster begins to fire, the sudden ejection of relatively high-pressure supersonic gas from a nozzle into a low-pressure environment generates a shock diffraction around the lip of the nozzle, resulting in lateral vortex formation. This phenomenon has

not been studied in any great detail, particularly under rarefied flow conditions such as those found in LEO. Generally, there are three issues related to the diffracted shock and the lateral vortex loop formation and propagation: sound generation, transport and mixing, and vortex interactions³⁸. The low Reynolds number, as a result of the low density, in a rarefied gas will influence the sound field generated from the vortices. The sound pressure level and sound frequency spectrum will be significantly different to that generated in a continuum gas and may cause unexpected vibrations. Secondly, the ejected gas from a nozzle contains some solid particles and liquid droplets. There is a possibility that these fast-moving particles and droplets may impinge on the surfaces of satellites and spacecraft downstream of the thrusters or against surfaces parallel to the thruster axis with the help of the shock diffraction and the vortex loop. It has been reported that these droplets and particulates can significantly influence operations on the International Space Station²⁵ and satellites²⁸, but the transient flow phenomena that cause the contamination or erosion and the resulting reduction of service life are not fully understood. It is also necessary to understand the propagation ability and coverage of a vortex loop with rarefaction effects to improve the thrust vector control. Even if the propulsion system used is a cold gas thruster, the lack of knowledge of rarefied transient flows could lead to an improper estimation of disturbing forces and heat loads. If multiple thrusters are deployed, shock interactions and vortex interactions will occur, and these complicated phenomena cannot be well understood without fundamental knowledge of rarefied vortex loops.

Typical examples can be found not only in the nozzle of micro-thrusters but also in the pulsed discharge of thrusters of spacecraft for attitude and orbit control and adjustment²². The flow from a convergent-divergent

^{a)}Electronic mail: z.cao.2@research.gla.ac.uk

^{b)}Electronic mail: Craig.White.2@glasgow.ac.uk

^{c)}Electronic mail: kostas.kontis@glasgow.ac.uk

micro-nozzle will experience flow-regime variation from the continuum regime ($Kn < 0.001$) within the combustion or stagnation chamber, to the slip and transition flow regime ($0.01 < Kn < 10$) as the flow expands in the diverging section, to the free-molecular regime ($Kn > 10$) far downstream of the nozzle exit²⁰. The Knudsen number Kn here is defined as

$$Kn = \frac{\lambda}{L}$$

where λ is the gas mean free path and L is a characteristic length scale. In the limit of continuum flow, a shock wave will diffract around the corner of the nozzle exit lip as the flow establishes, and the vortex sheet will roll up to form a vortex loop. However, if the mean free path at the nozzle exit is large enough, or the physical size of the nozzle is small enough, the high Knudsen number will influence the flow development.

In the continuum flow regime, shock wave diffraction and compressible vortex loop formation and development have attracted attention for decades. Brouillette and Hébert⁴ examined the propagation and interaction of compressible vortex loops with Mach numbers ranging from 1.0 to 2.0 using shadowgraph and schlieren photography. They classified the compressible vortex loop structure according to the shock Mach number. If the shock Mach number M_s is lower than 1.43, then there is no shock wave in the vortex loop, if $1.43 \leq M_s \leq 1.6$ there is an embedded shock wave, and if $M_s < 1.6$, a secondary vortex loops form ahead of the primary vortex loop.

Sun and Takayama⁴⁶ numerically studied the circulation production in shock wave diffraction around convex corners. They suggested that the vorticity increases with the wall angle and that there is a surge of vorticity at the corner with angles from 15° to 45° , with the vorticity tending to a constant value when the wall angle exceeds 90° . The vorticity produced by the slipstream is considered a vital portion of the total vorticity.

Shear layer development in shock wave diffraction was reported by Skews *et al.*⁴³. The authors enlarged the fluid domain outside the shock tube exit to allow for a longer time scale and avoid reflections of expansion waves and incident shock waves. They reported the existence of a lambda shock and suggested that the angle between the shear layer and the wall changes during the shear layer development when the wall angle is larger than 20° , which indicates that it is not self-similar.

Gnani *et al.*¹¹ employed splitters with a spike-shaped structure to produce shock diffraction and visualized the shock and turbulence phenomena using schlieren photography. They observed that the reflected shock waves were distorted during the process of passing through the vortex, but remained continuous and were not cut off by the vortex. The interactions between shock wave diffraction and a jet with two incident Mach numbers were investigated for noise control applications¹² at a Reynolds number greater than 1 million. It was found that the co-flow stretched the shock wave in the flow direction, and the rounded splitter generated small periodic vortices.

There are also some novel investigations of shock wave diffraction, such as diffraction from a curved exit from the shock tube²⁹, the interaction of two perpendicular diffracting shock waves⁴⁴ and vortex merging caused by shock wave diffraction in three dimensions⁶.

The studies outlined above are limited to the continuum regime, with Knudsen number $0 < Kn < 0.001$, in which the Reynolds number is high and the flow is often idealised as inviscid, and therefore the Euler equation can give a reasonably accurate model of the flow. However, under rarefied flow conditions, viscous effects remain important²⁷.

In rarefied conditions, shock waves have been investigated numerically using various techniques, such as direct simulation Monte Carlo (DSMC), kinetic solvers, and by hybrid numerical methods in shock tubes^{36,49,52}, hypersonic flows^{7,13,14,39-41}, and in plasma flow²⁶. Investigations of nozzle exit jet flow in the rarefied condition are mainly restricted to steady-state flow, such as hybrid numerical simulation of rarefied supersonic flow from micro-nozzles by Torre *et al.*²⁰, rarefied nozzle flow by Deschenes and Grot⁸, and transition regime flow in a diffuser investigated by Groll¹⁶. To the best of the authors' knowledge, there are no reports of transient effects during shock diffraction in the rarefied flow regime.

Therefore, this work will present an investigation of shock wave diffraction around a 90° corner under rarefied conditions with lateral vortex loop formation. The rarefaction effect on the shock wave diffraction at a Mach number of 1.6 will be discussed. The results from a continuum solver utilising slip and jump boundary conditions and a rarefied gas flow solver will be compared. To resolve the inner movements of fluid elements in a vortex, the vortex or vortex vector⁴⁷ is used in this work.

B. Usage of vorticity

Conventionally, a vortex is defined as a relatively high vorticity region and the strength of a vortex is quantified by the circulation Γ ⁴⁷, which is the sum of the vorticity within a closed loop in the flow domain. However, this definition is ambiguous, and in some circumstances, the vorticity concentration can not be explained to be the existence of a vortex, e.g. in turbulent flow. It is unable to distinguish between rotational and irrotational structures, but both rotation and local shear movements can create vorticity. For instance, in the boundary layer of laminar flow, there is a velocity gradient along the wall's perpendicular direction so that the vorticity in this area is non-zero, but no vortex exists. In Ref.47, the building of the vortex vector or vorticity is not derived from the continuum assumption of fluid flow so that vorticity is a purely mathematical concept and can be used in both continuum and rarefied flow.

The introduction of the vortex vector can effectively separate the vorticity $\vec{\omega}$ into a rotational part, vorticity

\vec{R} , and an irrotational part, the shear vector \vec{S} , such that

$$\vec{\omega} = \vec{R} + \vec{S}. \quad (1)$$

Compared with the former eigenvalue-based vortex identification criteria, including Q-criterion and λ_{ci} -criterion, the vorticity is a vector that will not be contaminated by the shear movements and flow visualisation benefits from the vorticity field and vorticity lines⁹. Since the new concepts are defined purely mathematically, and the calculation is based on linear algebra, there are no assumptions related to the fluid. Hence, the concepts are appropriate for all flow conditions.

II. NUMERICAL METHODS

A. Direct simulation Monte Carlo

The direct simulation Monte Carlo (DSMC) method³ is a standard tool for investigating rarefied flows with moderate to high Knudsen number. It has been used to simulate a wide range of rarefied flow problems, such as hypersonic vehicles³⁰, rarefied jets²³, multiphase plumes¹⁸, and even astrophysical flows⁵⁰.

DSMC is a particle based stochastic method that emulates the physics of real inter-particle processes and can provide a solution to the Boltzmann equation. A large number of real atoms/molecules are represented by each statistically representative simulator particle, which reduces the computational cost of a simulation. Additionally, the movements and collisions between representative particles are decoupled over a small time step, which is a valid assumption so long as the timestep remains much smaller than the local mean collision time of the gas. Gas-surface interactions, e.g. a diffuse reflection, are handled during this movement phase.

Once all of the particles have been moved, a stochastic collision process takes place. The collisions must take place between particles that are near-neighbours in order to obtain a realistic transfer of mass, momentum, and energy. In order to enforce this, a computational mesh is used, in which the cells must be smaller than the local mean free path of the gas. The computational cells are also used to obtain volumes that are necessary to report on flow properties such as density and temperature.

An overview of the basic algorithm that all DSMC solvers follow can be given as:

1. Update the position of all particles in the fluid domain using the particle tracking algorithm, which also deals with the motion of particles across faces of the mesh, and applies boundary conditions. Letting \vec{r} represent the particle's position, \vec{v} its velocity, and Δt the timestep, the mathematical form of the movement for the i -th particle is:

$$\vec{r}_i(t + \Delta t) = \vec{r}_i(t) + \vec{v}_i(t) \Delta t = \vec{r}_i(t) + \Delta \vec{r}$$

2. Prepare for the collision routine in each cell of the domain by updating the list of particles in each cell.
3. Perform the collisions based on the collision partner selection and binary collision models.
4. Sample the particle properties.
5. Go back to step 1 with the addition of Δt in time until the end time is reached.
6. Calculate the macroscopic properties of the flow field⁵¹.

In this work, the *dsmcFoamPlus* solver, developed by White *et al.*⁵¹ and implemented in OpenFOAM, is used. Transient flow simulations are performed, in which the algorithm above is performed for each individual case in the ensemble. Some additions to the *dsmcFoamPlus* solver have been implemented to make it possible to perform multiple ensembles of the same simulation. These are described in Appendix VI A.

As previously mentioned, in order to ensure near-neighbour collisions, the cell size should be smaller than the local mean free path. The virtual sub-cell technique is used in *dsmcFoamPlus*, in which the numerical cells are split into 8 individual collision cells. The number of particles in each cell must be sufficient to reduce the statistical error in the computed collision rates; typically at least 20 particles per cell are required when using the no time counter (NTC) method to calculate the number of possible collision pairs⁴². The number of DSMC particles in each cell can vary due to differences in local number density, and the cell size throughout the domain. Alternative collision schemes comprise simplified and generalized Bernoulli Trial^{34,45} collision schemes (SBT and GBT), but for simplicity and as a preliminary investigation, we only consider the NTC method in this work.

The number of ensembles M to obtain a desired fractional error in the local velocity E_u for each transient case in the DSMC method is determined according to the local flow Mach number Ma ¹⁷ and is given by

$$M = \frac{1}{\gamma Ac^2 N_{ppc} Ma^2 E_u^2}, \quad (2)$$

where γ is the ratio of specific heats, Ac is the acoustic number, and N_{ppc} is the average number of DSMC particles in the cell. In the current work, Ac can be approximated to 1. For instance, to obtain a 10% uncertainty in the velocity for nitrogen gas at a Mach number of 0.1, 286 ensembles with 25 particles in each cell are required. If the Mach number is increased to 0.3, the fractional error reduces to 3.33%. The fractional error of the other volume-averaged quantities of interest; density E_ρ , temperature E_T , and pressure E_P , can be evaluated by

$$E_\rho = \frac{1}{\sqrt{MN_{ppc}}} \frac{1}{Ac}, \quad (3)$$

$$E_T = \frac{1}{\sqrt{MN_{ppc}}} \sqrt{\frac{k}{c_v/N_A}}, \quad (4)$$

and

$$E_P = \frac{Ac\sqrt{\gamma}}{\sqrt{MN_{ppc}}}, \quad (5)$$

respectively.

B. Navier-Stokes-Fourier Solver

The *hy2Foam*⁵ solver is a density-based Navier-Stokes-Fourier code, designed to solve hypersonic flow problems, which can be characterised by high Mach number and the presence of chemical reactions. A two-temperature model assumes the translational and rotational temperature is equal to a trans-rotational temperature, and that the electron, electronic energy, and vibrational energy temperatures are equal to a vibrational-electron-electronic temperature. It is specially designed to simulate high-speed flow in the near continuum regime, which is computationally expensive with a DSMC solver. It has been verified and validated with and without chemical reactions in hypersonic flow conditions⁵. It is derived from the *rhoCentralFoam* solver and is therefore based on the central-upwind differencing schemes of Kurganov and Tadmor. A detailed description of *hy2Foam* can be found in Ref. 5.

Behind a shockwave with high Mach number, the gas molecules may, in general, have enough energy for the vibrational mode to become excited and for chemical reactions, such as dissociation, to take place. The Mach numbers are relatively low in the current work; hence, the two-temperature model will be degraded to a conventional single temperature. The temperature behind the shock wave will not be high enough to promote chemical reactions. Due to the Knudsen numbers considered, the no-slip boundary condition is not appropriate and so the Maxwell velocity slip⁵ and the Von Smoluchowski temperature jump boundary conditions⁵ will be used to model the velocity slip and temperature jump phenomena at the solid wall boundaries. Due to the small length scales and relatively low density, the Reynolds number is small, so the flow can be considered laminar.

1. Mesh and time-step independence

As the *hy2Foam* solver is based on the conventional computational fluid mechanics (CFD) method, a mesh and time-step independence study of vortex loop formation caused by a shock wave diffraction from a shock tube at $Kn = 0.005$ and $Ma_s = 1.6$ with different mesh level and time-step conditions is carried out to ensure that the discretisation errors have been minimized. The computational geometry is shown in Figure 1. The time

Table I: Mesh and time-step independence study.

Case label	Mesh name	Grid resolution (mm)	Time-step (s)
A	Coarse	1.0	5×10^{-8}
B	Medium	0.33	5×10^{-8}
C	Fine	0.25	1×10^{-7}
D	Fine	0.25	5×10^{-8}
E	Fine	0.25	2.5×10^{-8}

derivative is discretised using a first-order implicit Euler scheme and a second-order central-upwind differencing scheme is applied to discretise the gradient terms, divergence terms, and diffusive terms, and also to interpolate the cell centre values to the cell faces.

Three levels of mesh density and time-steps were simulated, as shown in Table I. The axial pressure distribution at a time of 0.1 ms has been plotted in Figure 2. No significant difference between the results of mesh density in cases B and C is found. Since the fine mesh is not computationally expensive, and the spatial resolution is better, the fine mesh with a resolution of 0.25 mm is used in the remainder of this work.

As the results with all time-steps in cases C-E are in good agreement, as shown in Table I, a time step of 5×10^{-8} s is chosen for all the *hy2Foam* cases to guarantee that the Courant–Friedrichs–Lewy number in all CFD cases is around 0.1.

2. Validation of vorticity calculator code

The calculation of the vorticity fields generated in this work is validated by studying a Burgers vortex superposed on a shearing motion⁹. The Burgers vortex is an exact solution of the Navier-Stokes equation, and its velocity field is described by

$$u = -\xi x - \frac{\Gamma}{2\pi r^2} \left(1 - e^{-\frac{r^2 \xi}{2\nu}}\right) y - C \frac{\text{Re} \xi}{\tilde{r}_0^2} y,$$

$$v = -\xi y - \frac{\Gamma}{2\pi r^2} \left(1 - e^{-\frac{r^2 \xi}{2\nu}}\right) x,$$

$$w = 2\xi z$$

where ξ is the strain rate, ν is the kinematic viscosity, and the last term on the right hand side of the x -component of velocity is a shearing motion superposed on to the vortex field. C is a user-defined constant, Re is the Reynolds number which is defined as $\text{Re} = \Gamma/(2\pi\nu)$, \tilde{r}_0 is a non-dimensional vortex size, equal to 1.5852. In the validation, $C = 1$, $\text{Re} = 10$, $\xi = 1$, and the circulation is specified as $63 \text{ m}^2/\text{s}$. The spatial resolution in the XY plane is 250×250 .

Contours of constant vorticity are shown in Figure 3(a) and agree well with the results in Figure 3(b) from

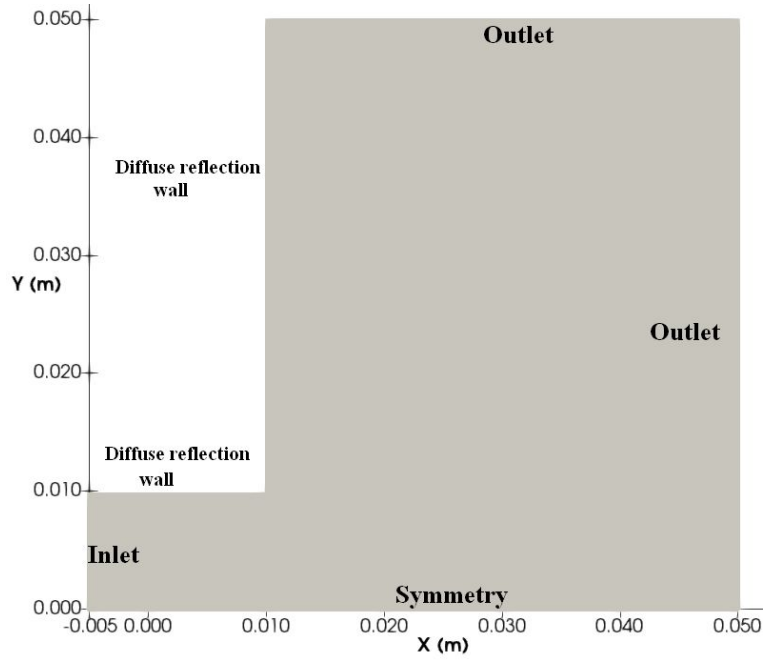


Figure 1: The computational domain used to perform the simulations.

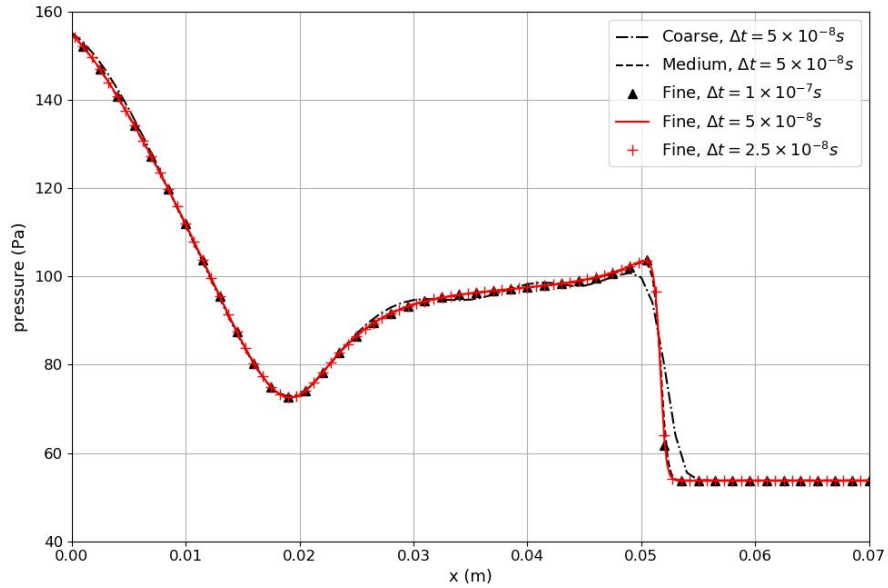


Figure 2: Axial pressure distribution at $t = 0.1$ ms, for different mesh densities and time steps.

Ref. 9. The vorticity here is in the z -direction so that x - and y - components are zero. Figure 4 is plotted along $x = 0$ in Figure 3(a), and shows that the sum of the z - component of vorticity and shear vectors is equal to the z - component of the vorticity vector, proving the accuracy of the vorticity calculator that has been implemented in the current work. The detail of pre-

processing of the calculator can be found in Appendix B, and the code can be found at <https://github.com/Kevin-Cao-gla/TransientDSMC-and-Rortex-scripts>.

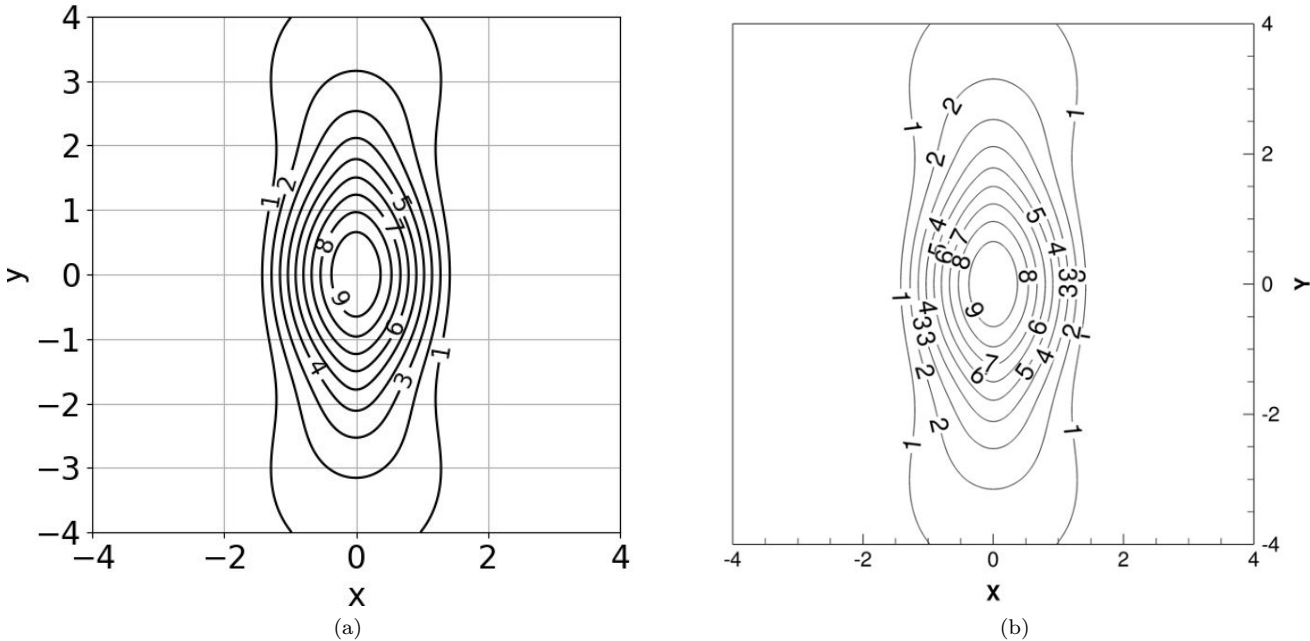


Figure 3: Comparison of contours of constant vorticity in a Burgers vortex in XY plane calculated from (a) the rorticity calculator used in the current work, and (b) from AIP-owned journal: "Reproduced from Ref. 9, with the permission of AIP Publishing."

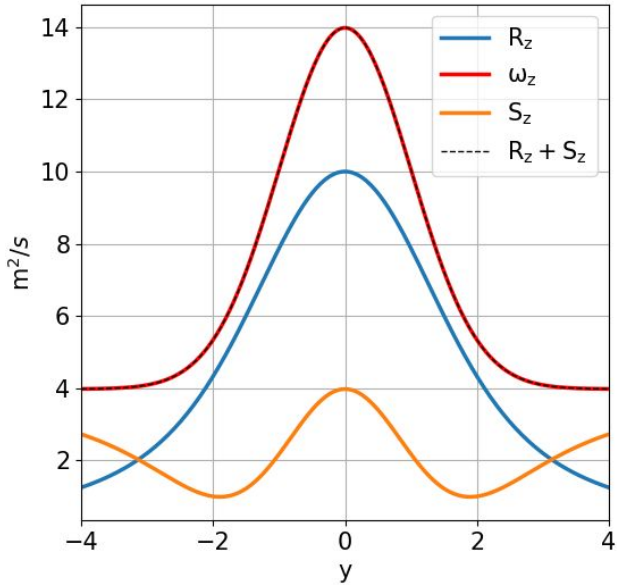


Figure 4: z -component of vorticity ω_z , rorticity R_z , shear vector S_z , and the sum of the rorticity and shear vector $R_z + S_z$ along a 1D line through the Burgers vortex.

III. SIMULATION DETAILS

The working gas in all simulations of this work is nitrogen, and the non-dimensional parameters, including the Knudsen number and the Reynolds number, are based on the half-height of the shocktube, which is 0.01 m. The mean free path of the Knudsen number is calculated according to the conditions downstream of the primary shock wave inside the shock tube. The Rankine–Hugoniot relations are used to calculate the macroscopic parameters defined in each case of this work; the case setup is shown in Table II and III. In the *dsmcFoamPlus* solver, the NTC method is used for collision partner selection, and the variable hard sphere model with Larsen–Borgnakke energy redistribution (with an inverse rotational energy collision number of 5) is used to perform the collisions. Again, the planar 2D computational domain is shown in Figure 1. The size of the domain outside the shock tube exit is varied for different cases because the computational costs are different. For instance, the computational cost for the DSMC case of $Kn = 0.005$ is the most expensive, so the fluid domain outside the tube exit is the smallest.

IV. RESULTS AND DISCUSSION

A. Vortex loop structure

Figure 5 shows pseudo-schlieren images at $t = 0.16$ ms and $Kn = 0.005$ from *hy2Foam*, based on the normalised density gradient ($\nabla\rho/|\nabla\rho|_{\max}$) (the value is limited to 0.1 for visualization purposes). There is no visible shock structure within the vortex until the shock Mach number reaches 1.5. The shock-free structure of the vortex loop with a shock Mach number lower than 1.43, first observed by Brouillette and Hébert⁴, is still valid in the near continuum regime. When the shock Mach number reaches 1.5, a weak embedded shock wave is produced inside the vortex loop, and its strength increases with the shock Mach number, as can be seen in Figure 7. The comparison of the intensified schlieren images for $Kn = 0.005 - -0.05$, from *dsmcFoamPlus* is shown in Figure 6. The shock wave thickness at $M_S = 1.6$ predicted by DSMC is larger than that predicted by CFD and this was also observed in Ref. 7. It is well-known that shock wave thickness increases with flow rarefaction and that the Navier–Stokes equations are unable to capture this physics. As illustrated in experiments^{19 24} and simulations^{53 31}, the vortex-induced shock pair occurs due to the high-velocity magnitude within the shear layer of the primary vortex loop in the continuum flow regime. It can be seen that the vortex-induced shock pairs and oblique shocks within the primary vortex loop degenerate and disappear in the rarefied condition. Embedded shock waves and shear layers still exist in Figure 5 and Figure 6(a) in the near continuum flow regime. As the Knudsen number increases, the embedded shock and the shear

layer degenerate further. It can be concluded that the high rarefaction level will simplify the inner structures of the compressible vortex loop.

B. Characteristics of the flowfield

1. Velocity and pressure field comparisons

Figure 8 shows the axial velocity and pressure distribution for $Kn = 0.005$ and $Kn = 0.025$ with $Ma_S = 1.6$ at $t = 0.16$ ms from both *hy2Foam* and *dsmcFoamPlus*. The axial velocity and pressure distributions from the two solvers are in good agreement in the near continuum regime, although again the CFD underestimates the primary shock wave thickness compared with that of DSMC.

A parameter called local gradient-length Knudsen number was suggested by Boyd³⁷ to evaluate the local continuum breakdown extent, and an improved version was proposed in Ref. 5:

$$Kn_{GLL} = \max(Kn_{GLL-\rho}, Kn_{GLL-T}, Kn_{GLL-|V|}, 5 \times \frac{T_t - T_r}{T_r})$$

where $Kn_{GLL-\phi}$ is the local gradient-length Knudsen number based on macroscopic property ϕ , T_t is the local translational temperature and T_r is the local rotational temperature. The axial distribution of Kn_{GLL} is shown in Figure 9, and the positions of the discrepancies in Figure 8 coincide with the x - coordinate where high Kn_{GLL} is found in Figure 9. An increase in local Knudsen number can be found in the primary shock, embedded shock, and the expansion at the exit. Through the comparison between Figures 8 and 9, the difference of the results in Figure 8 between the two solvers can be explained. It is mainly due to the increase of local rarefaction level, especially in the primary shock and the embedded shock. In the expansion region of Figure 9, the rarefaction level in the case of $Kn = 0.025$ grows faster than that of $Kn = 0.005$, so the difference between the two solvers is more obvious in Figure 8(b).

The normalized axial pressure distribution at $t = 0.12$ ms is shown in Figure 10. Intuitively, the increase of Knudsen number causes attenuation and thickening of the primary shock wave and the weak embedded shock, as shown in Figure 6, which is significant in the slip flow regime ($Kn < 1$). The axial pressure distribution profile differs between the slip flow and the higher Knudsen number regimes. The shock wave strength decreases as the flow tends towards the transition regime. The significant normalized pressure gradient caused by the weak shock wave is only visible at $Kn = 0.005$, $Kn = 0.025$, and $Kn = 0.05$. The pressure distribution profile in the transition regime, $Kn = 1.25$ is remarkably similar to that of the free-molecule flow, $Kn = 12.5$; in both cases the flow expands smoothly, and the primary shock wave evident in the slip flow regime has degenerated to a smooth decrease of pressure.

Table II: DSMC case parameters.

Case number	1	2	3	4	5	6
Kn ^a	0.005	0.025	0.05	0.125	1.25	12.5
M_S^b				1.6		
V_{inlet}^c				277.7274		
Re_S^d	168.72	33.75	16.87	6.75	0.67	0.07
p_2^e	152.6314	30.3291	15.1645	6.0658	0.60658	0.06066
p_1^f	53.77	10.755	5.3775	2.151	0.2151	0.02151
n_{inlet}^g	2.8159×10^{22}	5.6323×10^{21}	2.8161×10^{21}	1.1265×10^{21}	1.1265×10^{20}	1.1265×10^{19}
n_{outlet}^h	1.39×10^{22}	2.7722×10^{21}	1.386×10^{21}	5.5443×10^{20}	5.5443×10^{19}	5.5443×10^{18}
T_2^i				390.0192		
T_1^j				281		
Time step Δt (s)				1×10^{-7}		
Number of samples	620	2000	2500	2205	2205	3000

^a Knudsen number

^b Shock Mach number

^c Inlet flow velocity (m/s)

^d Shock Reynolds number

^e Inlet pressure (Pa)

^f Outlet pressure (Pa)

^g Inlet number density (m^{-3})

^h Outlet number density (m^{-3})

ⁱ Temperature after shock (K)

^j Temperature before shock (K)

Table III: CFD case parameters.

Case number	1	2	3	4	5
Kn			0.005		
M_S	1.3	1.4	1.5	1.6	2.0
V_{inlet} (m/s)	151.1889	195.3248	237.3839	277.7274	427.273
Re_S	99.05	124.58	147.68	168.72	235.21
p_2 (Pa)	125.267	133.56	142.3375	151.6314	193.05
p_1 (Pa)	69.4	63	57.9	53.77	42.9
T_2 (K)	334.6352	352.569	370.9807	390.0192	474.1875
T_1 (K)			281		

2. Rorticity and shear vector field

We call the region formed by closed-loop streamlines the vortex atmosphere. Since the vorticity can be decomposed into a rorticity and a shear vector, the vorticity field around and within the vortex atmosphere can be decomposed into a rorticity field and a shear vector field and hence, the movement of a fluid element at a position with nonzero vorticity can be estimated. Figures 11 and 12 present contours of the rorticity field and streamlines before and after the formation of the isolated rorticity region, or rorticity loop cross-section, with different shock Mach numbers, in the near continuum flow regime, as calculated using *hy2Foam* and *dsmcFoamPlus*. Increasing the shock Mach number causes the shape of the rorticity loop cross-section to change comma-like shape to a mushroom shape. Interestingly, the fluid elements within the expansion fan are rotational, especially at the sharp corner. It is worth mentioning that the local strength

of fluid-rotation at the corner is greater than that of the vortex centre when the shock Mach number exceeds 1.4.

The high rorticity magnitude at the corner in the expansion fan indicates that a fluid element experiences a significant increase of rotational kinetic energy because the rorticity is defined as twice the fluid-rotational angular velocity, according to Equation (2.23) in Ref. 47. It may imply that the transformation from internal energy to kinetic energy due to expansion at a corner is realized through fluid-rotation.

Figure 13 shows the shear vector field when the rorticity loop has just become isolated from the rorticity sheet. The maximum magnitude of the shear vector has been limited between 2×10^3 to 5×10^4 m^2/s to aid field visualization. As expected, the strength of shear movements inside the boundary layer and the vortex sheet is higher than that within the vortex atmosphere.

An unexpected result is that the rorticity loop cross-section does not cover all the closed-loop streamlines, but

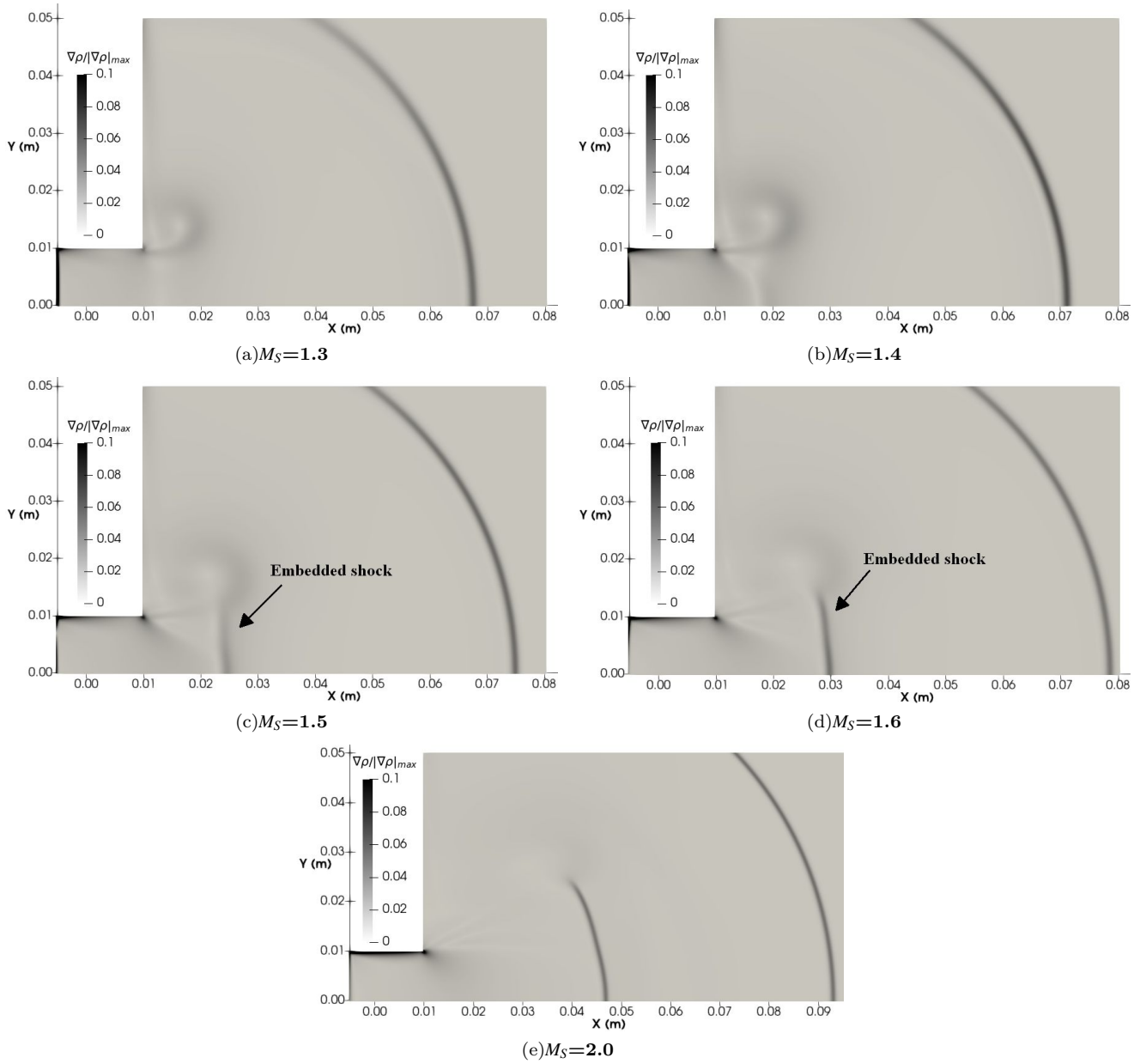


Figure 5: (a) (b) (c) (d) (e) **Comaprison of pseudo-schlieren images for $Kn = 0.005$ at $t = 0.16$ ms from the continuum solver.**

the core of the vortex atmosphere stays in the rorticity loop cross-section. Such a phenomenon can also be confirmed from the algorithm validation in the DNS simulation result of a 2D Blasius-profile mixing layer flow in Ref. 47. The rorticity field always coincides with the closed-loop streamlines if the vortex is stationary in the plane perpendicular to the rotational axis, such as in a Taylor-Green vortex sheet or a Burgers vortex, and it does not coincide with the closed-loop streamlines if the vortex translates.

The fluid elements in the periphery of the vortex atmosphere are dominated by shear movements, which can be observed in Figure 13. The vortex centre, defined from

the streamlines, is constrained within the circle of influence of the shear vector field, suggesting that the core of a vortex loop built on streamlines has both rotational and shear movements but the strength of the rotational movement is much stronger than that of the shear movement. Figures 12(a)- 12(d) indicate a reasonable agreement between the shape of the rorticity loop cross-section calculated with *hy2Foam* and *dsmcFoamPlus*.

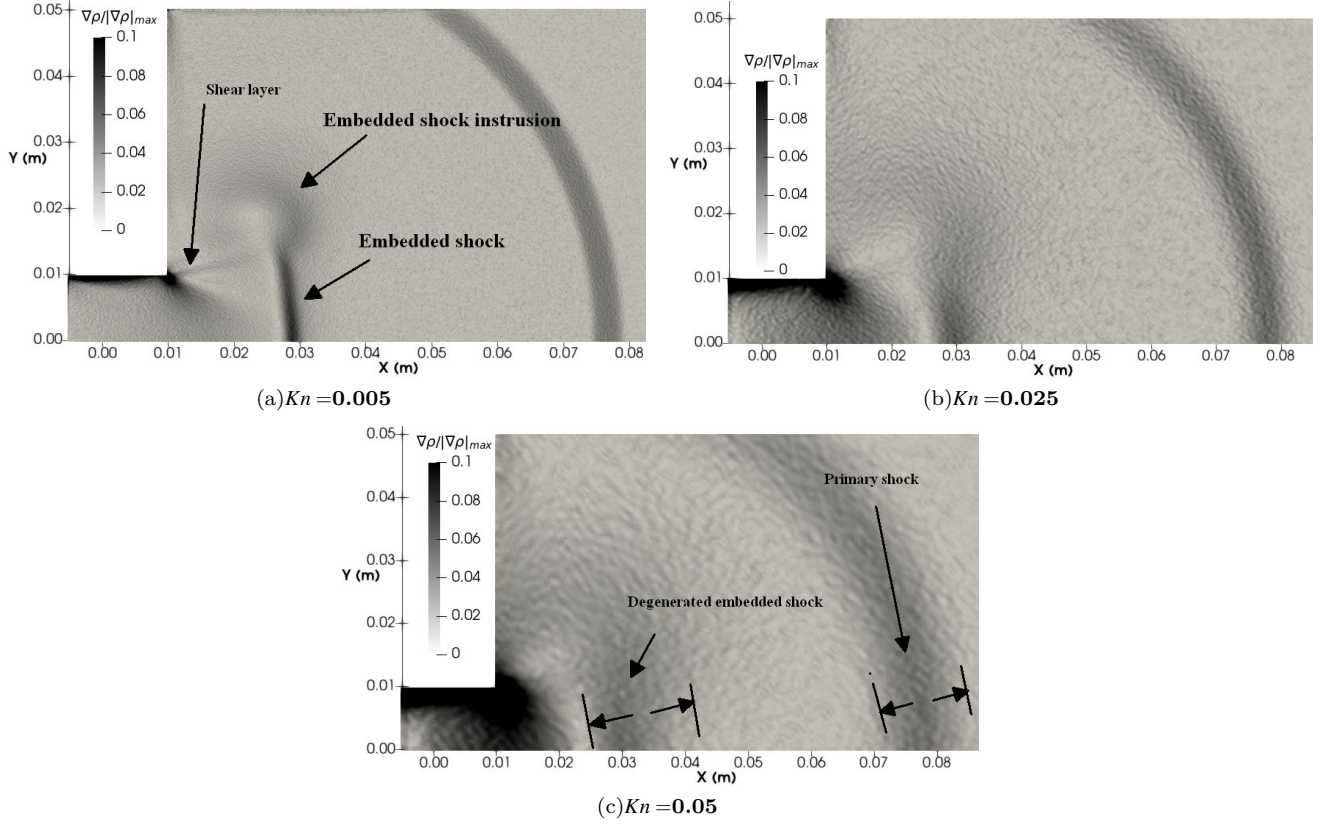


Figure 6: (a) (b) (c) Comparison of pseudo-schlieren images at $t=0.16$ ms for $M_S=1.6$ from the DSMC solver.

C. Evaluation of the rotational strength of the vortices

Circulation is a scalar quantity used to evaluate the strength of a vortex and can be defined as

$$\Gamma = \oint_L \vec{U} \cdot d\vec{l} = \int_A \vec{\omega} \cdot d\vec{A}. \quad (6)$$

The circulation is calculated by taking a closed circuit around the vortex atmosphere that includes the isolated vorticity region; an example of circuit ABCDA is shown in Figure 14.

With the introduction of vorticity, substituting Equation (1) into Equation (6), the following is obtained:

$$\Gamma = \int_A \vec{\omega} \cdot d\vec{A} = \int_A (\vec{R} + \vec{S}) \cdot d\vec{A}, \quad (7)$$

and thereby

$$\Gamma = \int_A \vec{R} \cdot d\vec{A} + \int_A \vec{S} \cdot d\vec{A}. \quad (8)$$

The decomposition in Equation (8) implies that the circulation includes parts that represent the rotational strength and shear strength of a vortex. The vorticity is a local vector describing the strength of the fluid-rotational

movement or rotational deformation at a specific position, and is unique at each point within the fluid domain⁴⁷. More importantly, the vorticity is parallel to the local rotation axis so that if a cross-section of a vortex is studied, this cross-section is fulfilled with the vorticity or, in other words, the vorticity lines will cross this cross-section. Subsequently, analogous to the definition of circulation, a new flux, called vorticity flux Φ_S , can be defined as

$$\Phi_S = \int_A \vec{R} \cdot d\vec{A}. \quad (9)$$

This flux quantifies the vortex rotational strength in a 2D plane in fluid dynamics. The vorticity flux can be used to estimate the potential of the propagation of a moving vortex. A moving vortex can propagate if the vorticity flux of this vortex is non-zero. The second term on the right hand side of Equation (8) can be defined as the shear vector flux

$$\Phi_S = \int_A \vec{S} \cdot d\vec{A}.$$

The dimensionless vorticity flux and circulation values are shown in Figures 15 and 16, respectively. The number of points for each Mach number is different because of the time delay of the formation of isolated vorticity

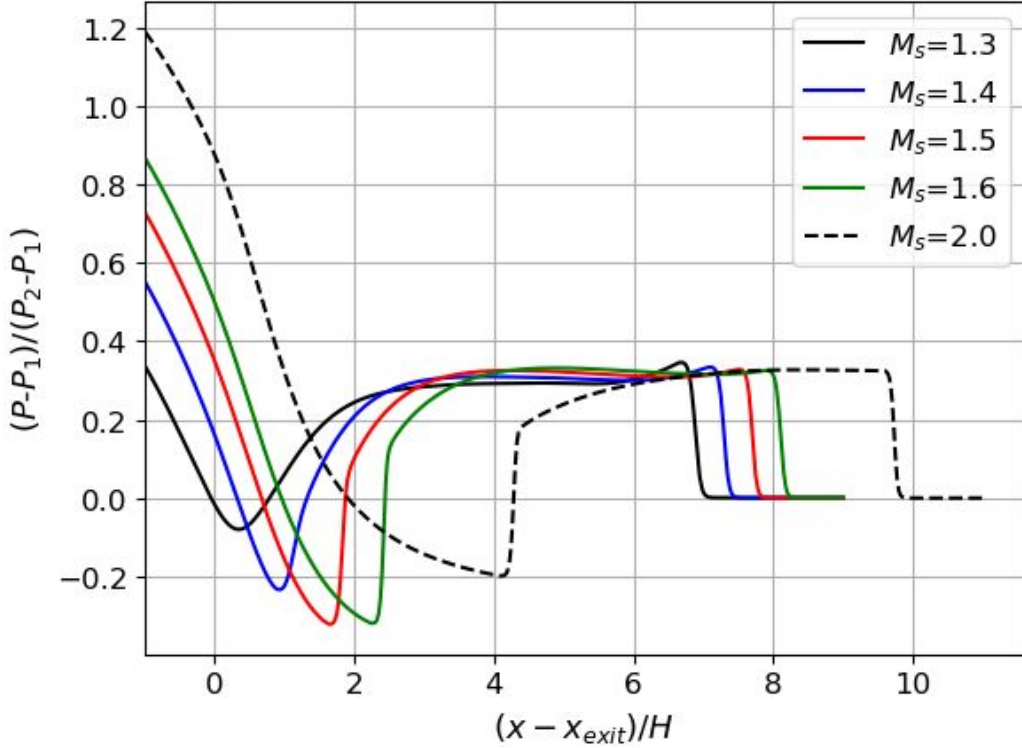


Figure 7: Dimensionless axial pressure distributions at $t = 0.19$ ms for different shock Mach numbers, as predicted by *hy2Foam*. x_{exit} is the x -coordinate of the shock tube exit.

loops at different Mach numbers. The postponement of the formation of the vorticity loop with the decrease of shock Mach number was shown in Figures 11 and 12, and the delay in the truncation could be caused by an insufficient accumulation of vorticity in the cases with lower shock Mach number. The non-linear growth of vorticity flux magnitude with time during the vortex formation process is not observed in the circulation, as shown in Figure 16, around the closed streamlines or vortex atmosphere². The non-dimensionalized vorticity flux profile changes when the shock Mach number exceeds a value between 1.4 and 1.5.

The decrease of the non-dimensionalized vorticity flux with the increase in Knudsen number from the two solvers are plotted in Figure 17 showing a decrease of vortex strength with increasing rarefaction. The DSMC results for $Kn = 0.005$ is an ensemble of 620 simulations and those for $Kn = 0.025$ and $Kn = 0.05$ are 2000 and 2500 ensembles, respectively. The results show that the vortex loop in the rarefied condition still propagates, especially the cases in the slip flow regime. It is apparent that the non-dimensionalized vorticity flux at $Kn = 0.005$ calculated by the DSMC method is reasonably coincident with that from CFD and the data of $Kn = 0.025$ and $Kn = 0.05$ are in excellent agreement. The reason for the small discrepancy in the near continuum regime should

be ascribed to the embedded shock intrusion shown in Figure 5(d), and 6(a). The strength of such an intrusion is too weak to be noticeable in Figure 5(d) from the CFD results, causing the velocity and the lateral velocity gradient difference around the vorticity loop, as shown in Figure 18. The weak embedded shock in the near continuum regime further degenerates and becomes too weak to influence the calculation of vorticity flux in the slip flow regime, as shown in Figures 6(b) and 6(c), rendering fair agreements in Figure 17.

The quantity of circulation includes both the surface integral of the vorticity and the shear vector. The value is much larger than that of vorticity flux due to the lack of movement-resolving ability of vorticity. Equation (8) allows the inner part of the circulation to be studied. Both rotational and shear movements of fluid elements within a vortex loop are of great importance to its formation and development. The calculation of the circulation of a vortex loop requires selecting a circuit along the symmetry axis¹⁵ and covering the so-called vortex atmosphere². Still, there are no strict rules on the limitation of this circuit size, resulting in the introduction of errors. One advantage of the vorticity vector is its ability to represent the fluid-rotational region of a vortex by using iso-surfaces with a clear boundary and therefore the strength of the fluid-rotational part of a vortex can be accurately

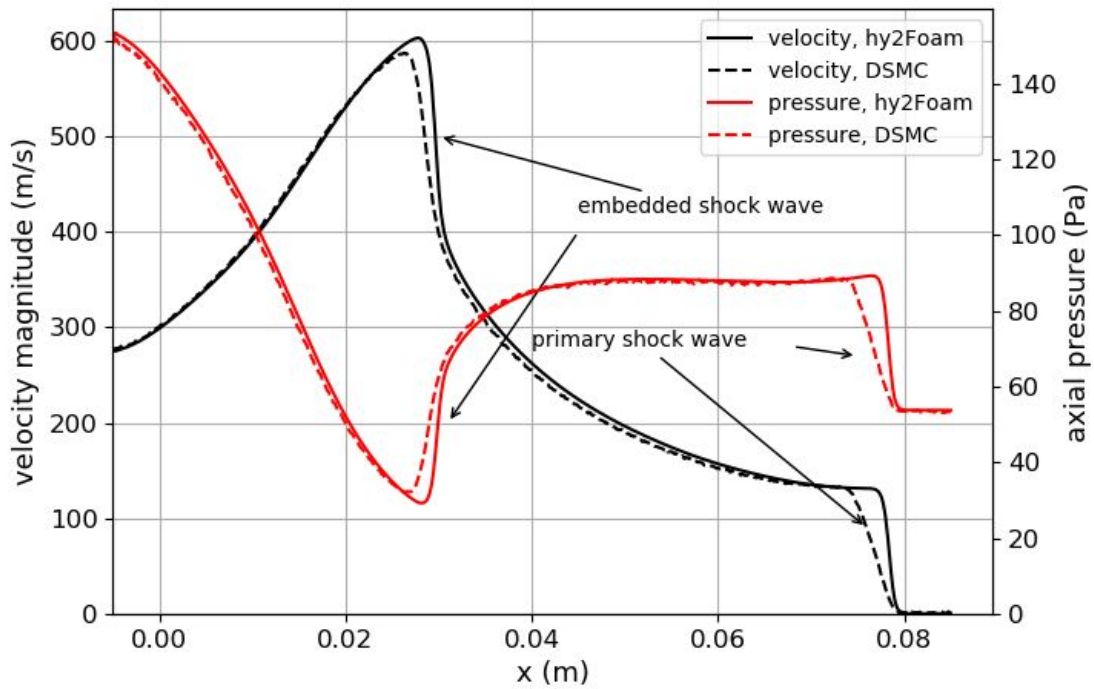
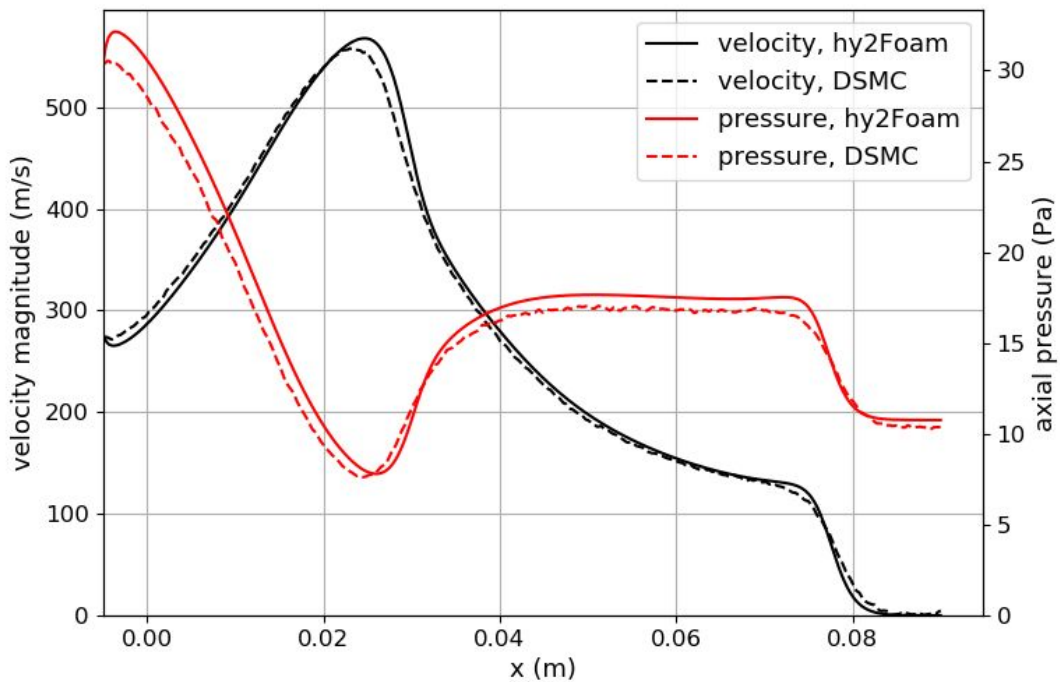
(a) $Kn=0.005$ (b) $Kn=0.025$

Figure 8: (a) (b) Axial velocity magnitude and pressure comparisons of the results from *hy2Foam* and *dsmcFoamPlus* at $t = 0.16$ ms for $Kn=0.005$ and $Kn=0.025$ with $Ma_s=1.6$.

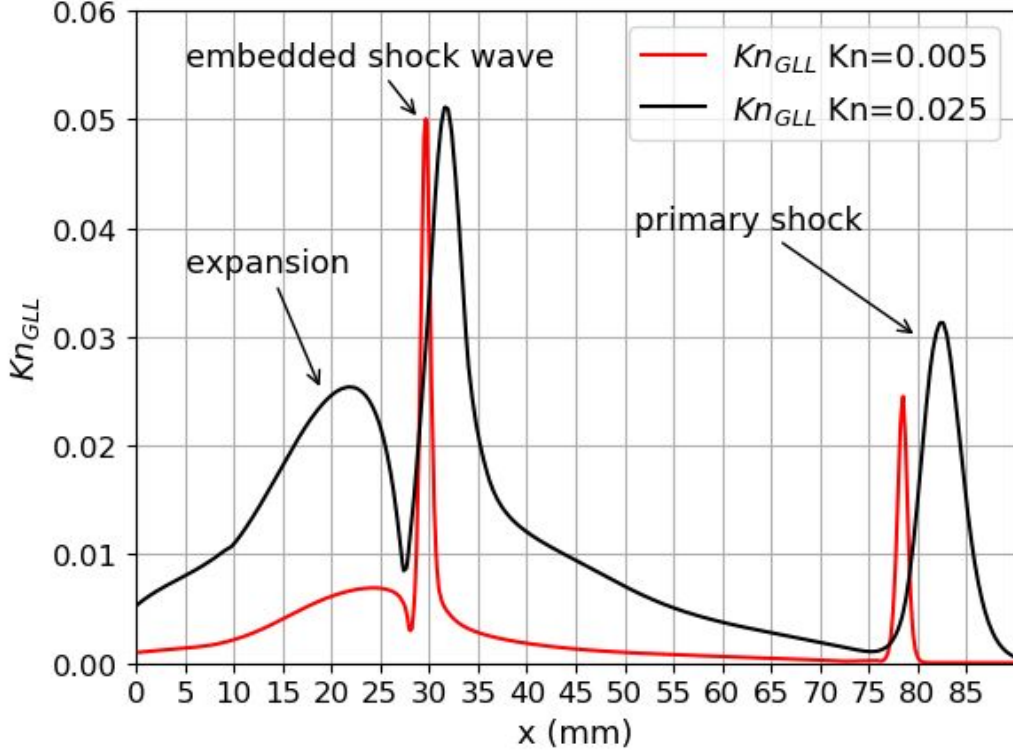


Figure 9: Axial Kn_{GLL} distribution of $Kn=0.005$ and $Kn=0.025$ from *hy2Foam*.

integrated and presented using the vorticity flux. By introducing vorticity, it can be established whether a fluid element at any point in time inside the flow domain of interest has either rotational or shear movement, increasing the physical understanding of the flow. In Figures 11 and 12, the vorticity magnitude field is cut off by setting a threshold of $1 \times 10^{-4} \text{ m}^2/\text{s}$, and a clear border of the vortex described by vorticity is captured, demonstrating that the fluid elements' movements can be effectively analyzed through calculating the vorticity.

A vortex sheet is generated before the formation process of the vortex loop near the tube exit. The vorticity within the vortex sheet can be decomposed into a vorticity sheet and a shear vector sheet according to Equation (1), as in Figures 11 and 13. The vorticity region within a vortex atmosphere is connected to the vorticity sheet at the tube exit (Figures 11(a), 11(c), 11(e), 12(a), 12(c) and 12(e)) and the connection is cut off a short time afterwards (Figures 11(b), 11(d), 11(f), 12(b), 12(d) and 12(f)). The sheet at the tube exit acts as an umbilical cord feeding vorticity into the vortex atmosphere. When this cord is truncated, the vorticity inside the vortex should decrease or remain constant. However, the gradual increase of vorticity flux presented in Figure 15 implies that there must be a source of vorticity leading to the continuous increase; this source may be the shear vector indicated in Figure 13. The shear vector sheet still

exists when the vorticity region inside the vortex loop is isolated so that the shear vector sheet feeds the total circulation of the vortex loop. It is easy to imagine that there is vorticity fed into the vorticity loop through the closed surface of the vorticity loop or the shear vector from the closed vorticity region's interior. However, the shear vector field surrounds the closed vorticity field.

Table IV shows the circulation, vorticity flux, and shear vector flux of an isolated vorticity region with $Kn = 0.005$ at $t = 0.20 \text{ ms}$ and $t = 0.21 \text{ ms}$. At $t = 0.2 \text{ ms}$, the vorticity flux is approximately $5.872 \text{ m}^2/\text{s}$; the shear vector flux is around $8.666 \text{ m}^2/\text{s}$, and the total circulation is $14.538 \text{ m}^2/\text{s}$, which means there is no internal vorticity source within the vorticity region. Hence, the increase of vorticity can only be attributed to the transformation from the shear vector to vorticity or, in other words, the conversion of movement from shear to fluid-rotation, $\vec{S} \rightarrow \vec{R}$. As shown in Figure 19, where the shear vector magnitude visualization is limited to $5 \times 10^4 \text{ m}^2/\text{s}$, the increase of the vorticity flux of the isolated vorticity region can only be fed by the shear vector sheet. According to Equation (8) at time $t = 0.2 \text{ ms}$ and $t = 0.21 \text{ ms}$, the circulation of the isolated vorticity region can be decomposed into

$$\int_{A_{0.2ms}} \vec{\omega} d\vec{A} = \int_{A_{0.2ms}} \vec{R} d\vec{A} + \int_{A_{0.2ms}} \vec{S} d\vec{A} \quad (10)$$

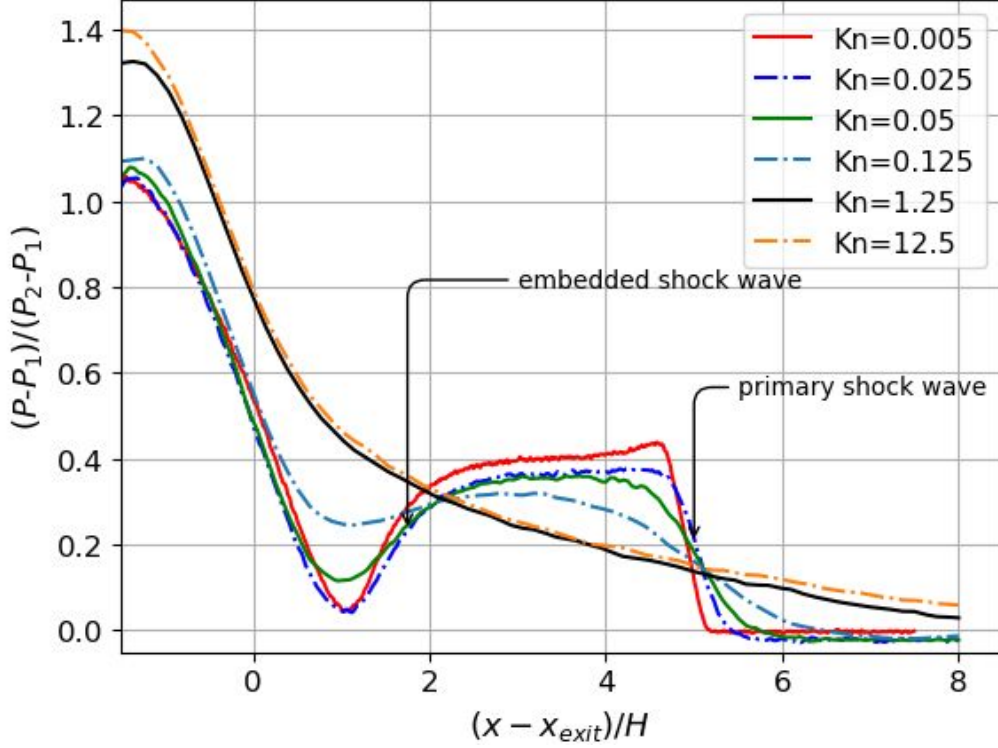


Figure 10: Rarefaction effect on normalised axial pressure distribution at $t=0.12$ ms by *dsmcFoamPlus*. x_{exit} is the x - coordinate of the tube exit.

Table IV: Circulation, rorticity flux, and shear vector flux of an isolated rorticity region at $Kn=0.005$ and $M_S=1.6$ calculated from *hy2Foam*.

Time (ms)	Circulation (m^2/s)	Rorticity flux (m^2/s)	Shear vector flux (m^2/s)
0.21	15.1134	6.039	9.0744
0.2	14.5383	5.8718	8.6665
Difference	0.5751	0.1672	0.4079

and

$$\int_{A_{0.21ms}} \vec{\omega} d\vec{A} = \int_{A_{0.21ms}} \vec{R} d\vec{A} + \int_{A_{0.21ms}} \vec{S} d\vec{A}, \quad (11)$$

where $A_{0.2ms}$ and $A_{0.21ms}$ are surface areas of the isolated rorticity region at 0.2 ms and 0.21 ms respectively. Subtracting Equation (11) from Equation (10) results in

$$\Delta\Gamma = \Delta\Phi_S + \Delta\Phi_R. \quad (12)$$

In Equation (12), the term on the left-hand side is the total circulation difference of the isolated rorticity region between two times. The first term on the right-hand side is the rorticity flux increment and the second term on the right-hand side is the shear vector flux increment. This equation is proved through the data in Table IV. As the circulation supply comes from the shear vector

sheet, the total circulation difference, $\Delta\Gamma$, is equal to the total shear vector flux injected into the isolated rorticity region boundary. Therefore, by moving the second term on the right-hand side of Equation (12) to the left-hand side

$$\Delta\Gamma - \Delta\Phi_S = \Delta\Phi_R \quad (13)$$

is obtained, and hence,

$$\Delta\Phi_{\vec{S}^T} = \Delta\Phi_R \quad (14)$$

where \vec{S}^T is the transformed shear vector. The left-hand side of Equation (13) is the difference between the total shear vector flux and the remaining shear vector flux within a rorticity loop. This difference is equal to the magnitude of the transformation from the shear vector flux to the rorticity flux. As shown in Equation (14),

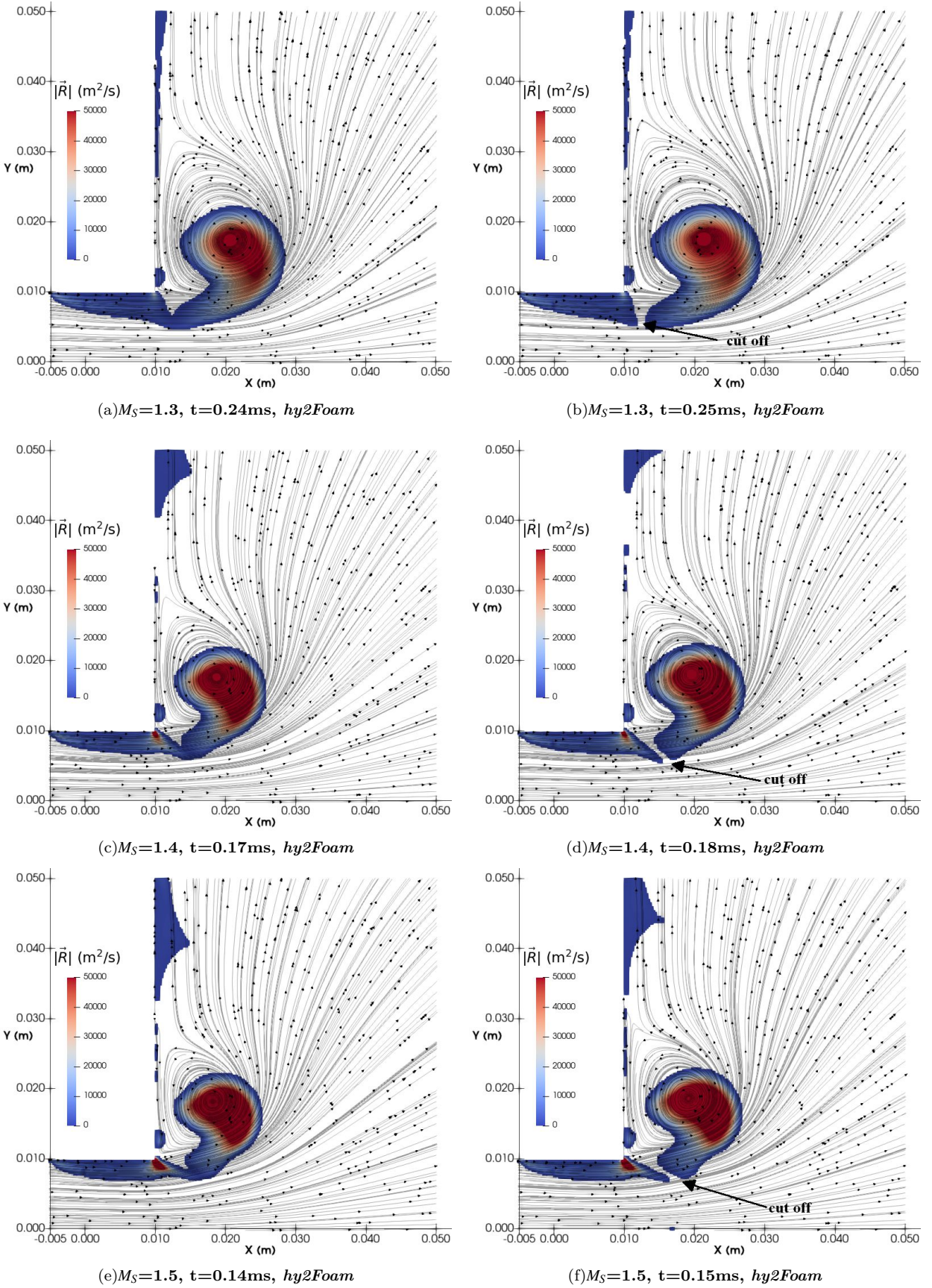


Figure 11: (a) (b) (c) (d) (e) (f) Rorticity magnitude field and streamlines calculated by *hy2Foam* at $Kn=0.005$ before and after the formation of isolated rorticity region. The rorticity magnitude, $|\vec{R}|$, is limited to $5 \times 10^4 \text{ m}^2/\text{s}$ to aid field visualization.

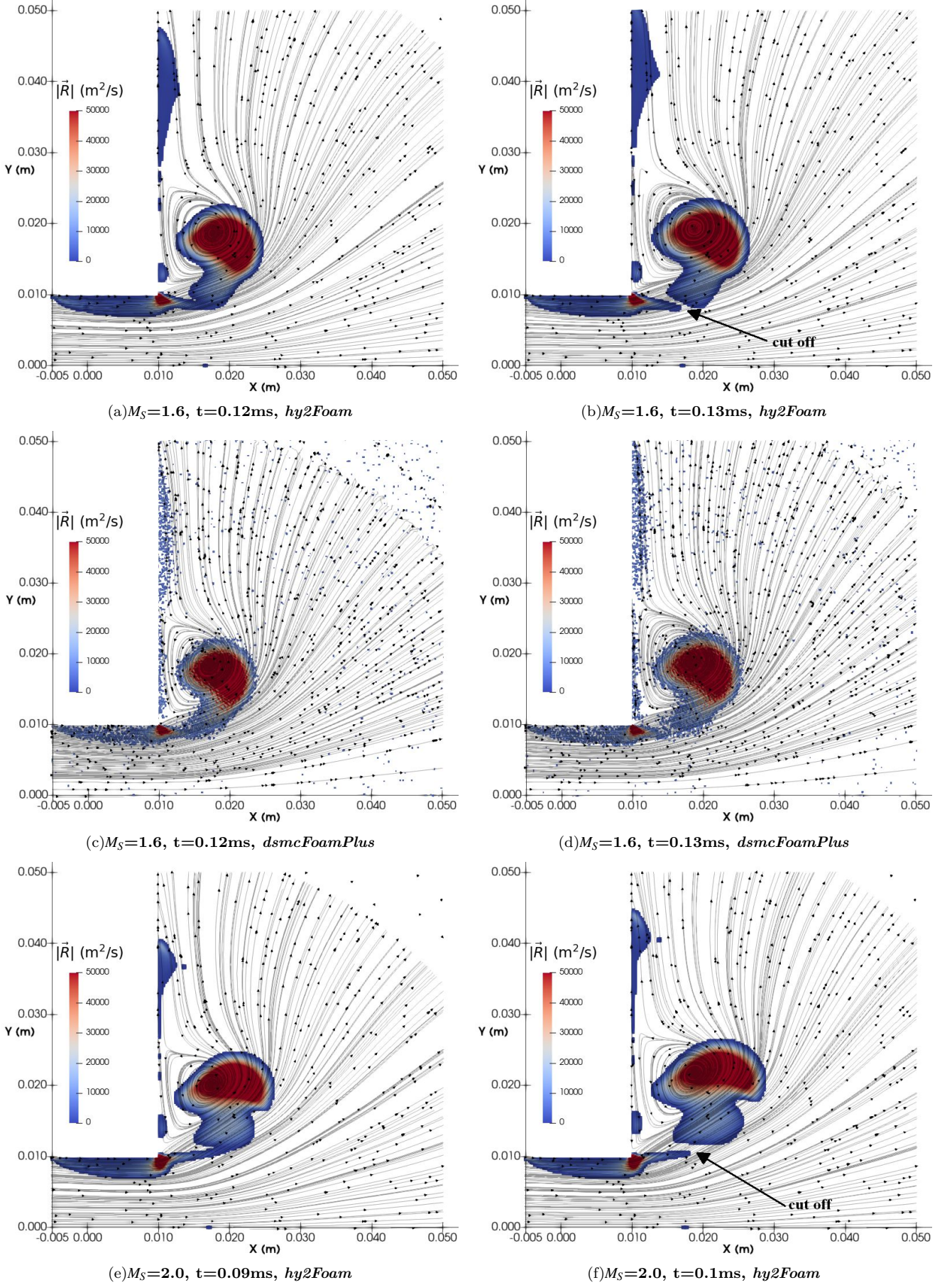


Figure 12: (a) (b) (c) (d) (e) (f) Rorticity magnitude field and streamlines calculated by *hy2Foam* with $\text{Kn}=0.005$ before and after the formation of isolated rorticity region. The rorticity magnitude, $|\vec{R}|$, is limited to $5 \times 10^4 \text{ m}^2/\text{s}$ and the lower limit of $|\vec{R}|$ in the *dsmcFoamPlus* results is $6800 \text{ m}^2/\text{s}$ to aid field visualization.

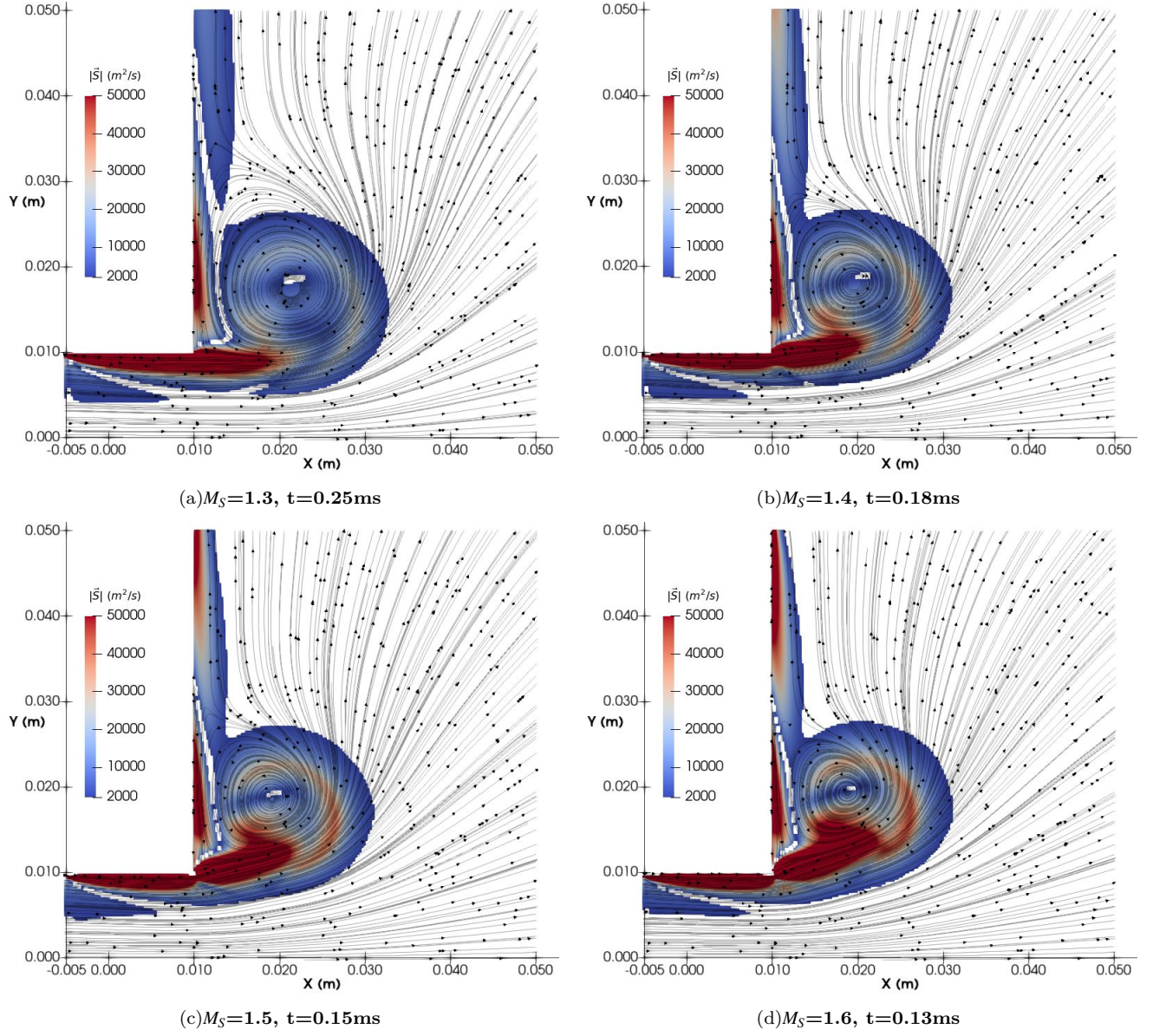


Figure 13: (a) (b) (c) (d) Shear vector field and streamlines calculated by *hy2Foam* with $\text{Kn}=0.005$.

the transformation magnitude of the shear vector flux is equal to the vorticity flux increment. If the conversion between two vectors does not exist, then the increase in circulation must be equal to that of the shear vector flux in Table IV, which decreases. Therefore, the decrease of shear vector flux within a closed surface is equivalent to the increase of the vorticity flux. This relationship is also implied in the divergence of Equation (1) with the introduction of vector identity in three-dimensions:

$$\nabla \cdot \vec{R} = -\nabla \cdot \vec{S} \quad (15)$$

Equation (14) is the absolute integral form of Equation (15). Equation (15) proves that there is a mutual transformation between the vorticity and shear vector, and the magnitude of the change is equivalent. This equation

is helpful in the understanding of phenomena related to vortex formation and development and turbulent flow.

D. Geometrical characteristics of rarefied vortex loop

Calculating the geometrical parameters of rarefied vortex loops is helpful in the understanding of the vortex loop coverage in the flow field. We can define the region with vorticity in the vortex described by streamlines as the rotational core of a vortex loop. As the vorticity field of a vortex loop core is an irregular shape, an equivalent diameter of a vortex is defined as

$$d_{eq} = \sqrt{\frac{A_R}{\pi}}$$

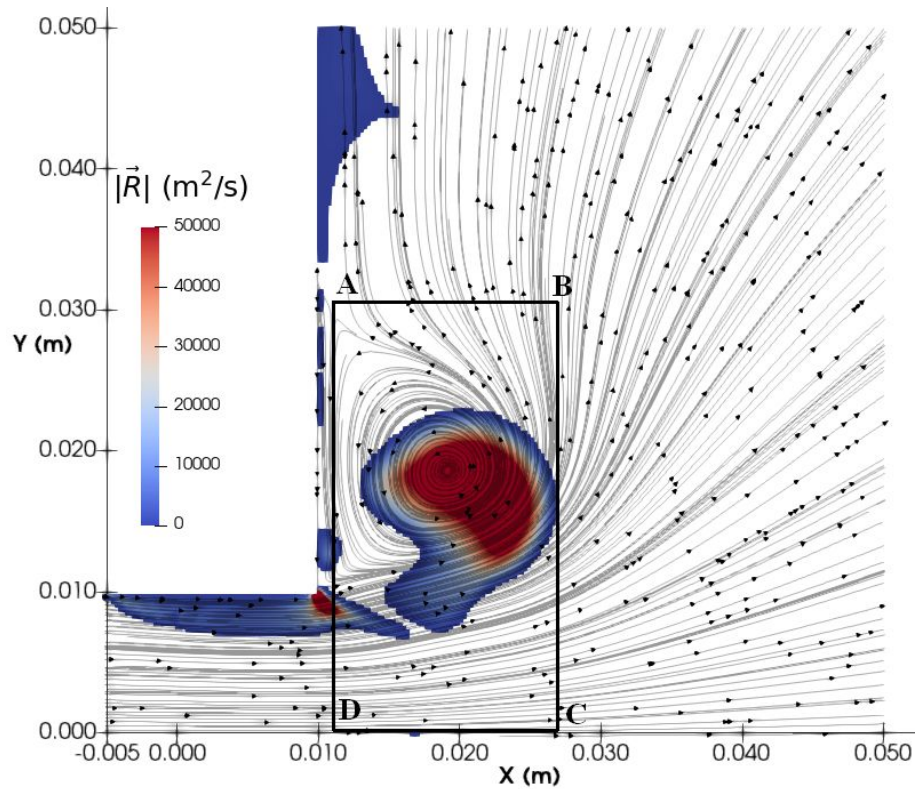


Figure 14: Circulation circuit.

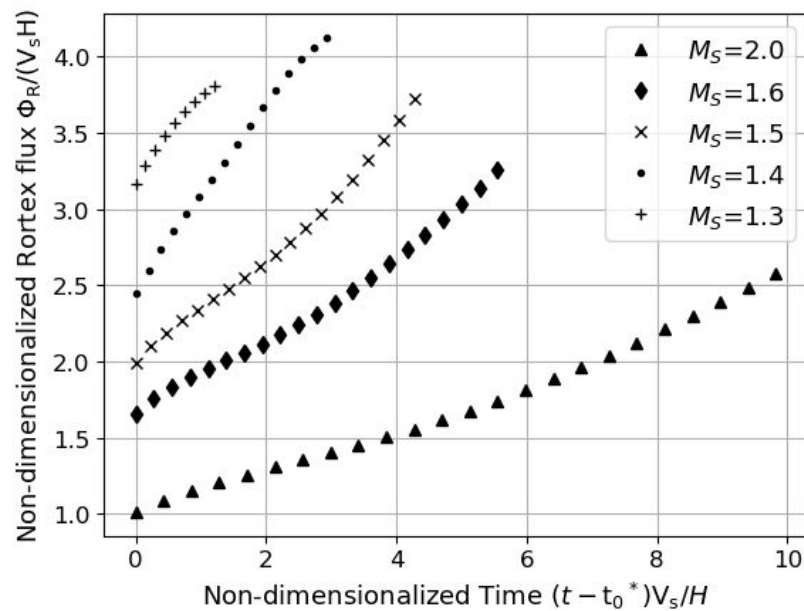


Figure 15: *hy2Foam* results of non-dimensional rorticity flux at $Kn=0.005$. V_s is the initial shock velocity inside the shock tube and H is the characteristic length, which is equal to half height of the tube. $t^* = \frac{(t-t_0^*)V_s}{H}$, where t_0^* is the time that the rorticity loop formed and it is 0.25ms, 0.18ms, 0.15ms, 0.13ms, 0.1ms for $M_s = 1.3$, $M_s = 1.4$, $M_s = 1.5$, $M_s = 1.6$, $M_s = 2.0$, respectively.

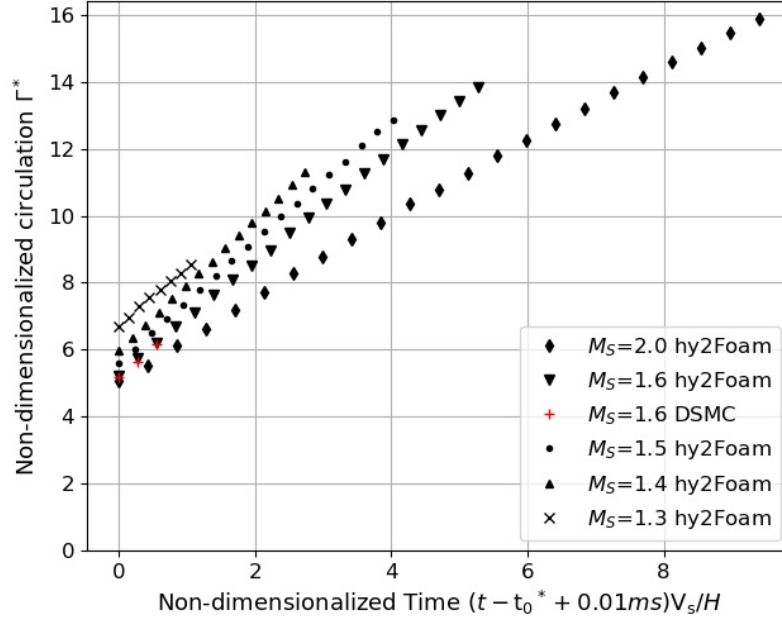


Figure 16: *hy2Foam* results of non-dimensional circulation of the vortex loop at $Kn=0.005$. $\Gamma^* = \Gamma/(V_s H)$

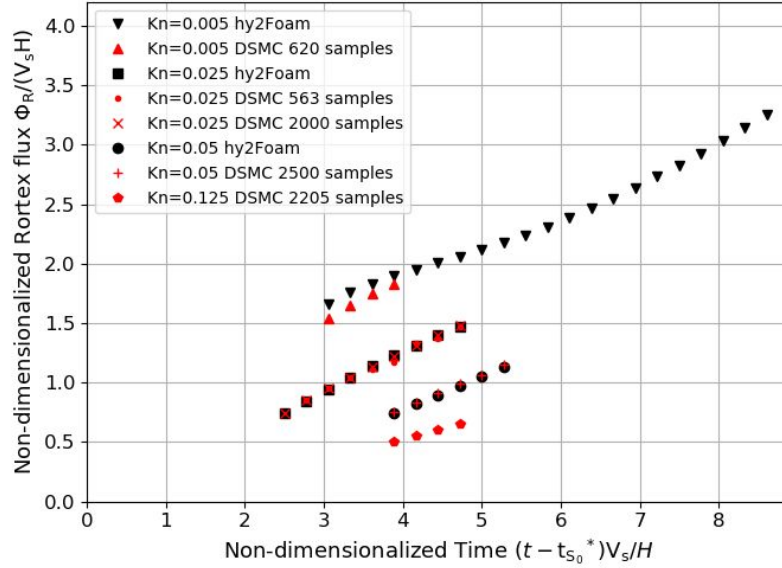


Figure 17: Non-dimensionalised rorticity flux for $M_S = 1.6$ by *dsmcFoam* and *hy2Foam*. $t_{S_0}^*$ is the time when the shock wave reaches the tube exit, and here it is equal to 0.02 ms.

where d_{eq} is the equivalent diameter of the rotational core of a vortex loop, and A_R is the area of the rorticity loop cross-section. This equivalent diameter intuitively describes the size of a circular ring’s cross-section with the same area. In Figure 20, the equivalent radius is non-dimensionalized by the characteristic length. The

non-dimensional time begins when the rorticity region within the vortex atmosphere is isolated from the rorticity sheet. When the shock Mach number is 1.4 and 1.3, a highly linear relationship between the equivalent radius of the rorticity ring and non-dimensional time is found. In contrast, the relationship becomes non-linear in the

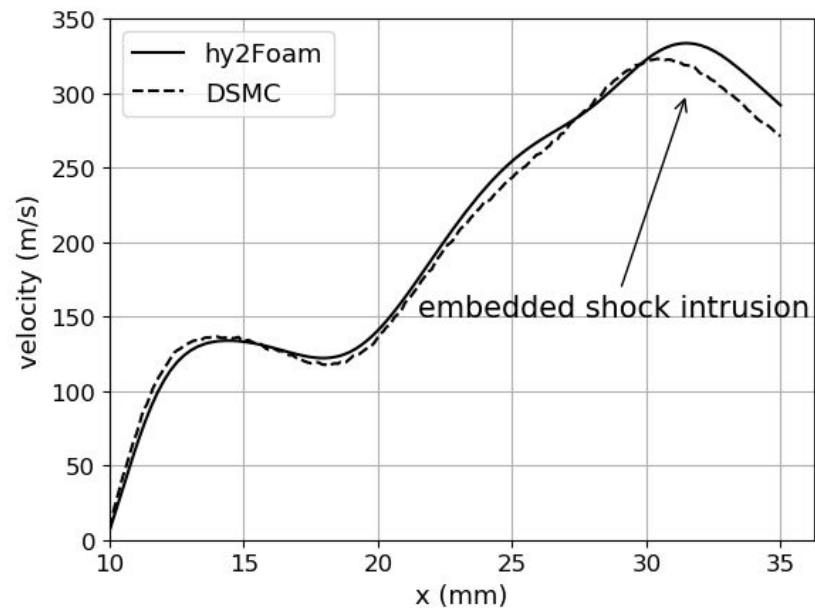


Figure 18: Velocity distribution at $y=17.5$ mm, $t=0.16$ ms with $M_S=1.6$ and $Kn=0.005$.

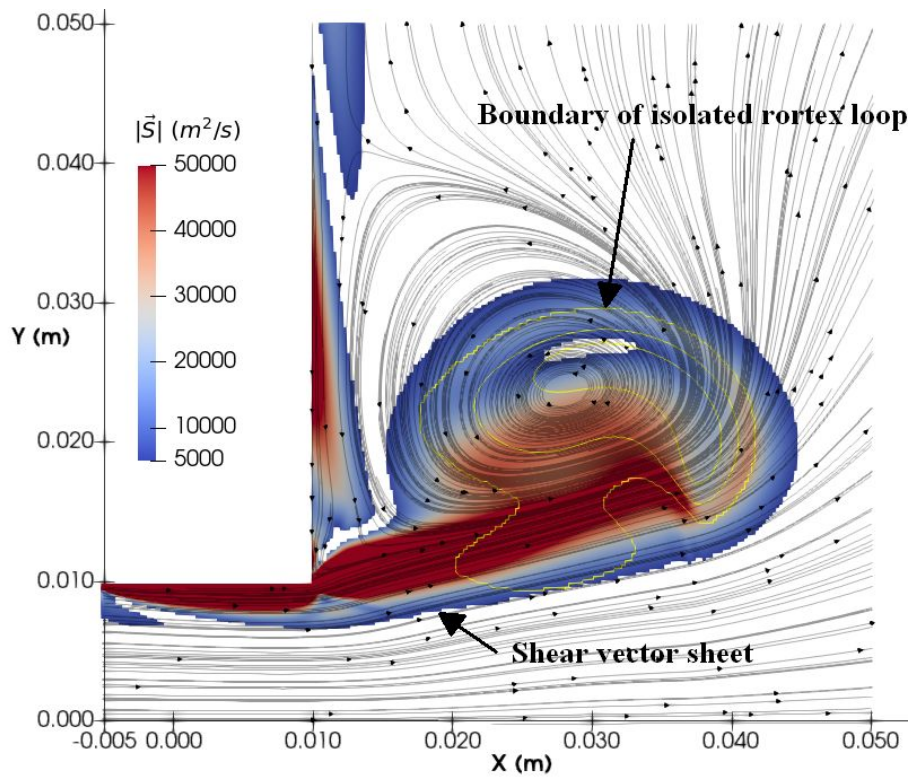


Figure 19: Shear vector field and vorticity contour of $Kn=0.005$ and $M_S=1.6$ at 0.21ms by *hy2Foam*. The closed yellow line is the boundary of the isolated vorticity loop generated from iso-surfaces.

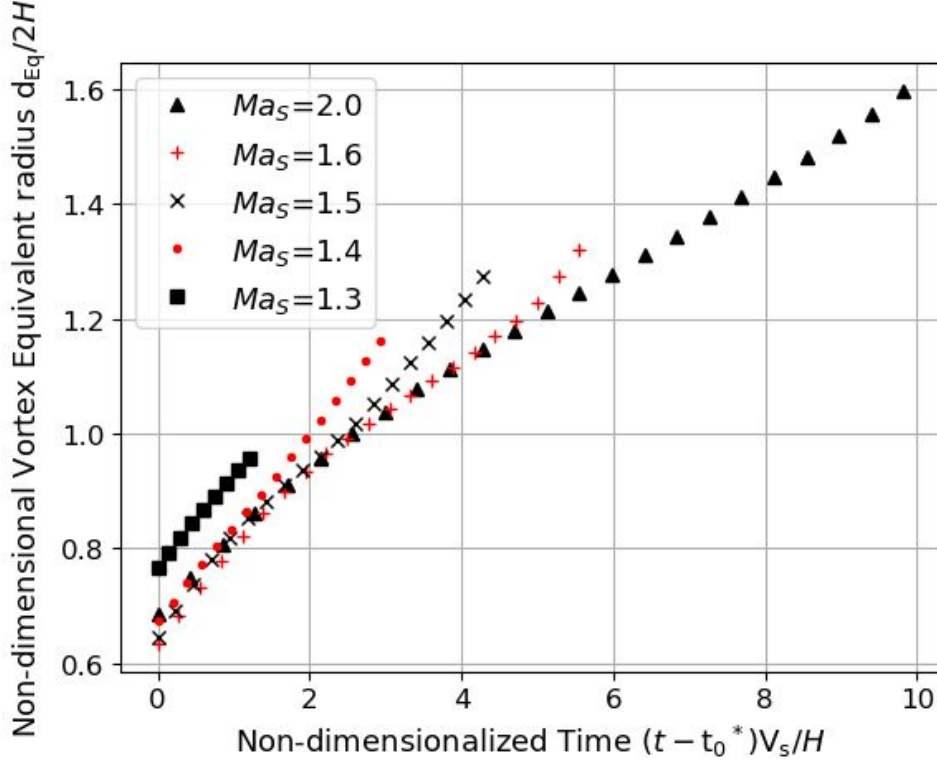


Figure 20: Non-dimensionalised equivalent radius at $Kn=0.005$, calculated with *hy2Foam*.

early stage of the formation process when the shock Mach number reaches and exceeds 1.5. During the formation of the vortex loop, there is a deceleration of the equivalent radius' growth rate when the shock Mach number reaches 1.5.

In general, calculating the centroid of the cross-section of a vortex loop is useful in evaluating its radius if such a vortex loop is a ring. Conventionally, the centroid of a vortex cross-section is based on the distribution of vorticity³². Here, the centroid of such a region can be calculated when vorticity components replace the vorticity.

The centroid of the vorticity loop cross-section in the XY plane is defined as:

$$x_{\vec{R}} = \frac{\int_A x \vec{R} d\vec{A}}{\int_A \vec{R} d\vec{A}} = \frac{\int_A x R_z dx dy}{\Phi_{\vec{R}}},$$

$$y_{\vec{R}} = \frac{\int_A y \vec{R} d\vec{A}}{\int_A \vec{R} d\vec{A}} = \frac{\int_A y R_z dx dy}{\Phi_{\vec{R}}}.$$

The dimensionless result of $y_{\vec{R}}$ is plotted in Figure 21, which can be considered the trend of ring radius growth if the loop is a ring. It is evident that the radial size of the vortex loop positively correlates with the shock Mach number. These fast-growing vortex loops may impinge on the surface perpendicular to a nozzle axis or rub against the surface parallel to the axis.

The radial component of the centroid with rarefaction effect is presented in Figure 22. A gradual growth of the semi-height of a vortex loop with increase of Knudsen number is found, but the difference in semi-height between the $Kn=0.005$ and $Kn=0.025$ is small. The expansion caused by low pressure outside the tube leads to growth of the vortex loop in the radial direction. The vortex loop formed in the slip flow regime has a larger size but lower strength. The propagation ability of the vortex ring in the rarefied condition remains to be investigated.

E. Failure of vortex loop formation

Figure 23 displays the variation of the velocity and the streamlines due to the increase of rarefaction level with a shock Mach number of 1.6 in the slip flow regime. A laminar flow pattern can be noticed in each case; the Reynolds number based on the semi-height of the tube is $Re_s = \rho V L / \mu$ and the result is shown in Table II. The laminar flow pattern in the DSMC simulations proves that the laminar-flow assumption applied in *hy2Foam* is appropriate.

For cases in the near continuum regime ($Kn=0.005$ and $Kn=0.025$), vortices can be found after the shock wave diffraction at the early stage, i.e. $t=0.07$ ms, whereas, at $Kn=0.05$, there is no vortex-like structure at the same

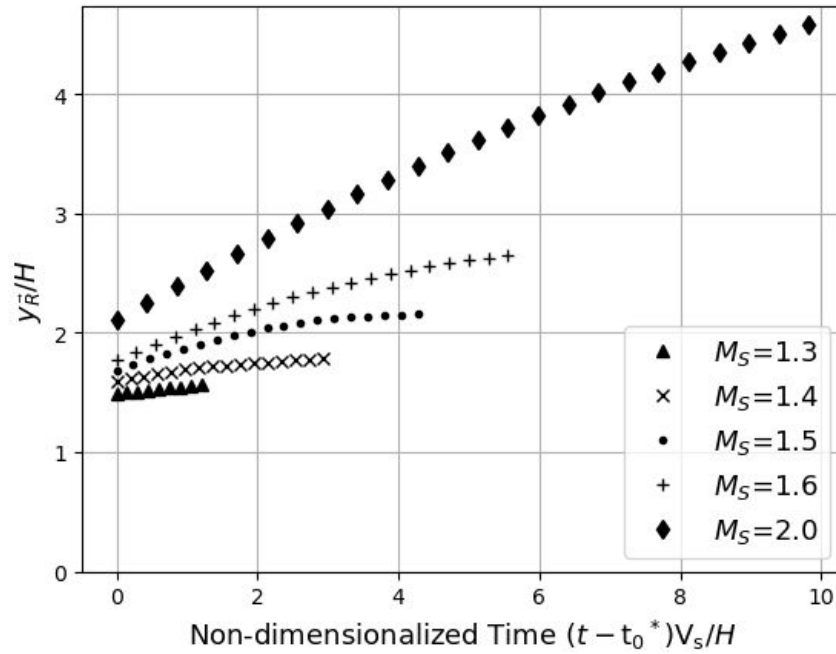


Figure 21: Dimensionless y - components of the centroid of the vorticity loop with time at $Kn=0.005$, calculated from *hy2Foam*.

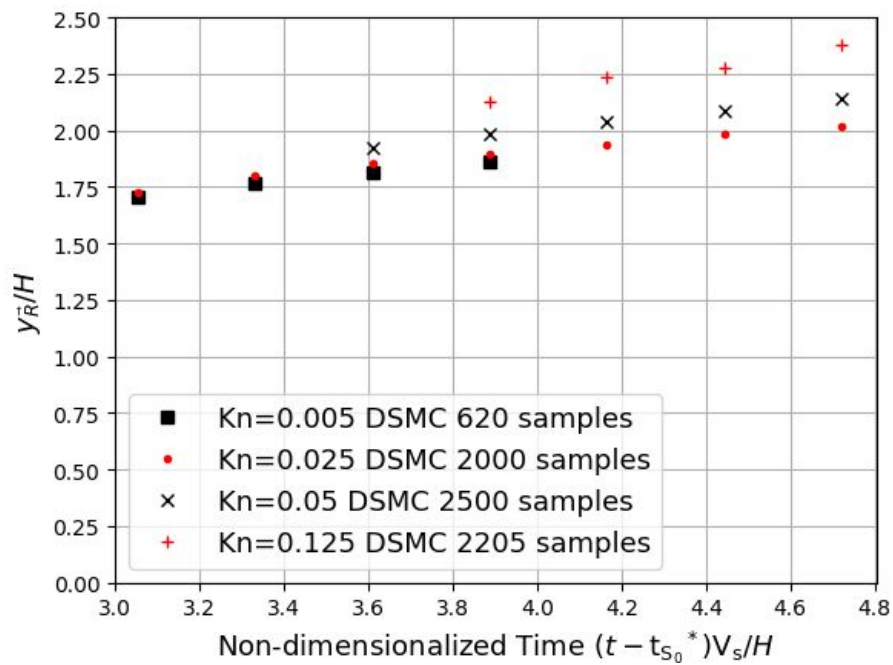


Figure 22: Rarefaction effect on dimensionless semi-height with $M_S = 1.6$. $t_{S_0}^*$ is the time when the shock wave reaches the shock tube exit, and here it is equal to 0.02 ms.

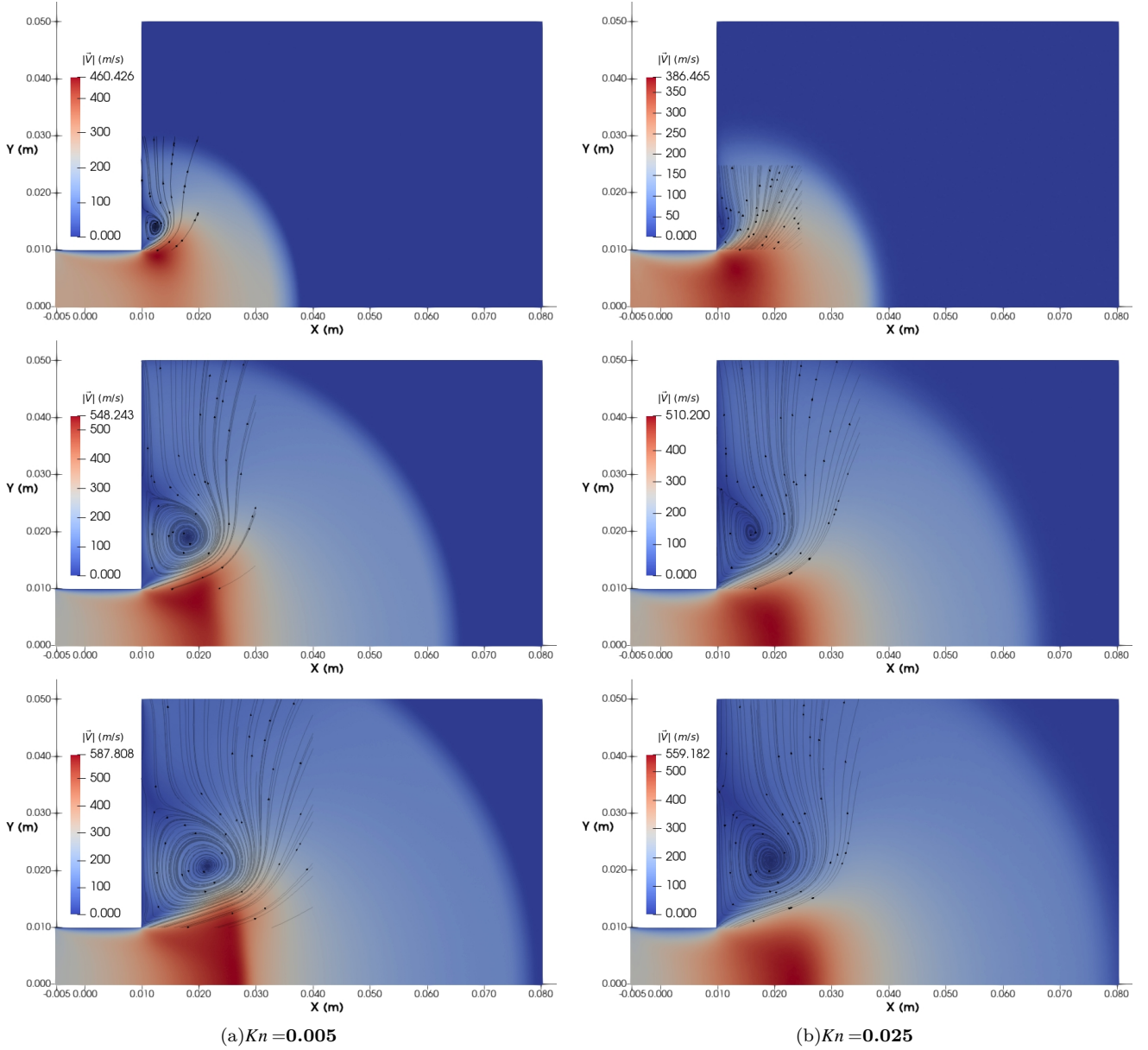


Figure 23: (a) (b) Velocity field and streamlines calculated by *dsmcFoamPlus* in the slip and transition flow regime ($t=0.07$ ms, 0.13 ms, and 0.16 ms) at $M_S=1.6$.

time. An indistinct vortex-structure at $t=0.16$ ms can be observed for the case of $Kn=0.0125$, indicating a time delay in the vortex formation caused by the rarefaction. When the flow enters the transition regime and free-molecule regime, no vortices form, as shown in Figure 25. An investigation of vortex formation at different levels of rarefaction can also be found in the validation of the DSMC method by Bird³. In contrast, in Bird's cases, the vortices formed were under subsonic flow conditions, and the limitation of the Knudsen number for vortex formation is 0.88. This Knudsen number limiting the vortex formation was reduced to 0.82 in the work of Ahangar *et al.*¹ and 0.662 in Ref. 10. Therefore, there is a Knud-

sen number limitation of vortex formation and it may be a function of inlet flow conditions; however, the relationship between the specific Knudsen number of vortex formation limitation and the inlet flow condition is not fully understood. In addition, this limit will influence the propagation distance of a vortex loop. In the continuum flow regime, the vortex loop will entrain the atmosphere around it and grow in size, but in the rarefied condition, especially in the condition of low back pressure, there is insufficient gas atoms/molecules for the vortex loop to entrain. The vortex loop will be diluted during its propagation and should eventually disappear when the Knudsen number limit for formation is reached.

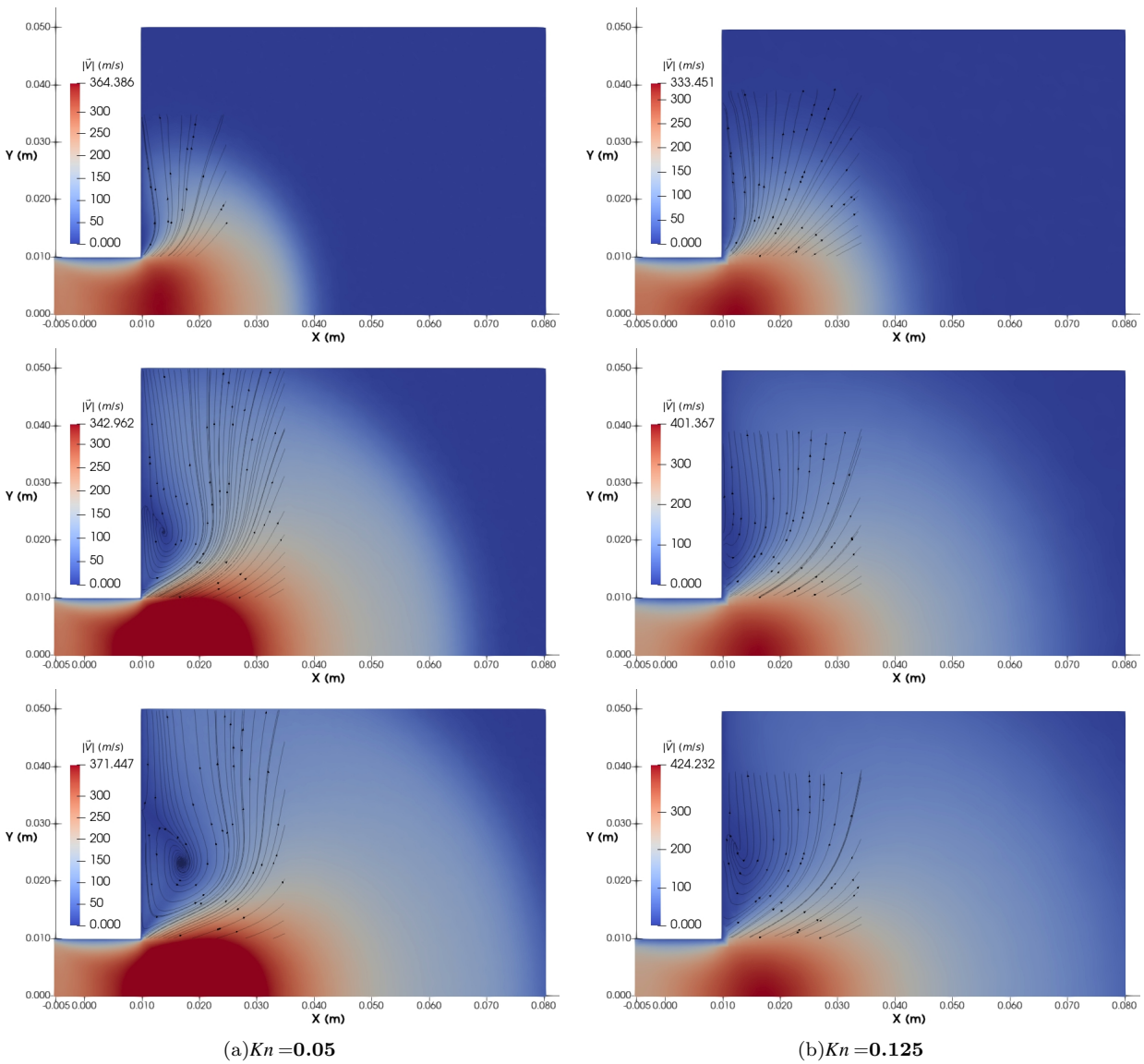


Figure 24: (a) (b) Velocity field and streamlines calculated by *dsmcFoamPlus* in the slip and transition flow regime ($t=0.07$ ms, 0.13 ms, and 0.16 ms) at $M_S=1.6$.

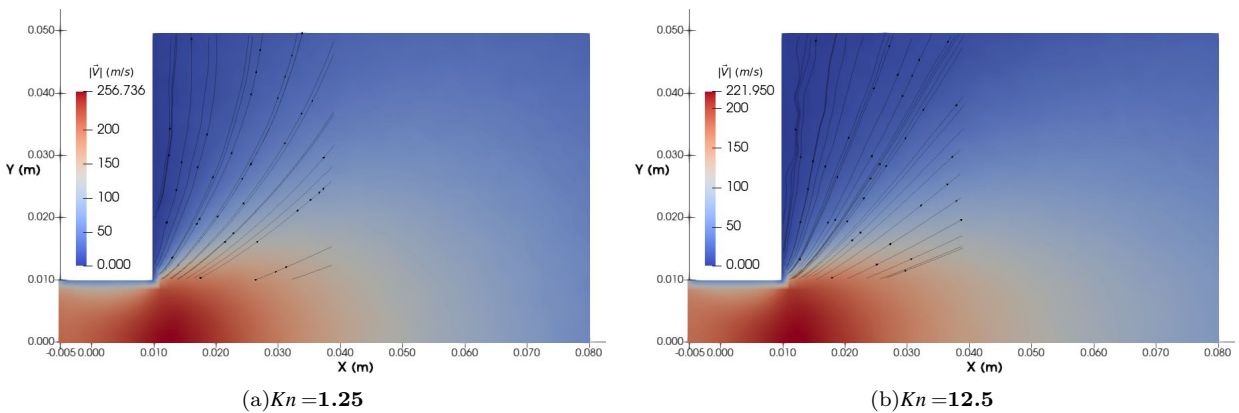
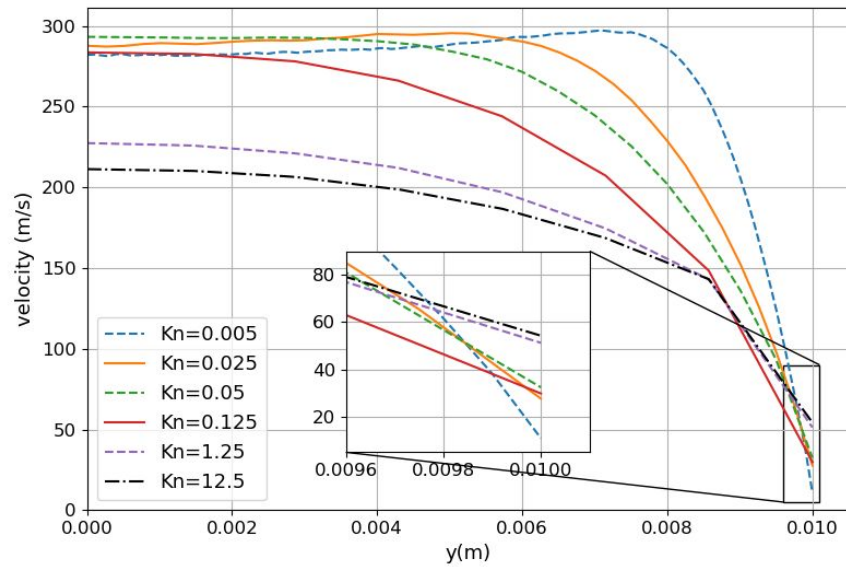
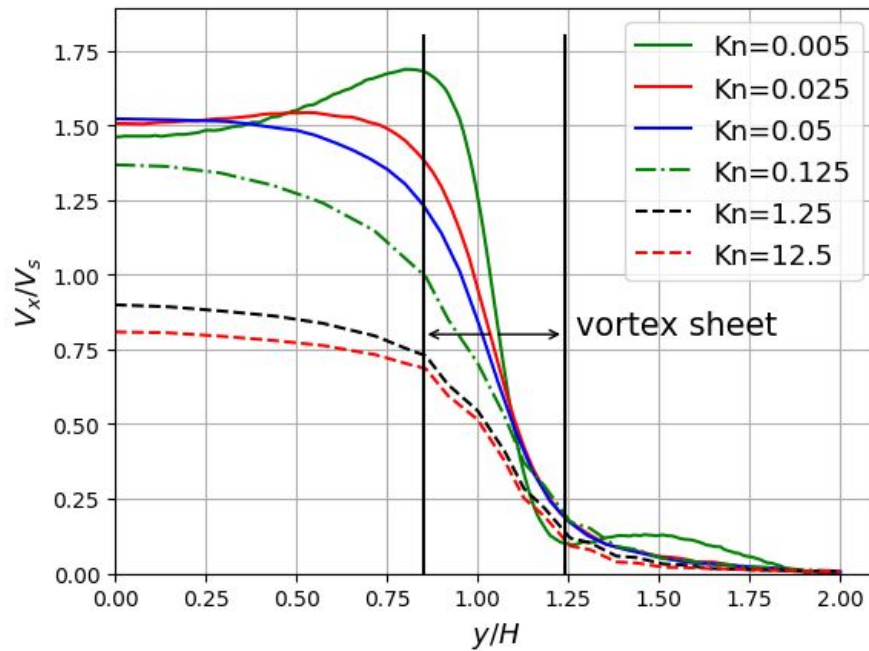


Figure 25: (a) (b) Velocity field and streamlines calculated by *dsmcFoamPlus* in the free molecule flow regime ($t=0.19$ ms).



(a)



(b)

Figure 26: (a) (b) Dimensionless velocity profile inside the shock tube at $x=2.5$ mm, $t=0.07$ ms for different Knudsen numbers from *dsmcFoamPlus* (a). Tangential velocity profile outside the shock tube at $x=12$ mm, $t=0.12$ ms for different Knudsen number with 1.6 shock Mach as calculated from DSMC (b).

The failure of vortex formation can be explained from the perspective of the vortex sheet³⁵. In continuum flow, a cylindrical vortex sheet with discontinuous tangential velocity is considered the precondition of a vortex loop, and the vortex sheet will subsequently roll up into spirals to form a vortex loop¹⁵. The boundary layer is of great importance in the formation of the vortex sheet, but the increment of the mean free path leads to the thickening of the Knudsen layer where the molecules have a higher collision frequency with the surface than with other molecules, as shown in Figure 26(a). The increase of the Knudsen number increases the velocity slip, resulting in higher wall velocity as can be seen in Figure 26(a).

Outside the tube, Figure 26(b) presents the dimensionless tangential velocity profile calculated from DSMC at $x=12$ mm, which is 2 mm away from the tube exit, and $t=0.12$ ms. The thickness of the vortex sheet increases, and the tangential velocity difference decreases significantly with an increase of the Knudsen number. The vortex sheet can be considered to be diluted with the increase of rarefaction level.

Therefore, the effect of a thicker Knudsen layer, indicating higher Δy , higher wall velocity, and smaller Δu results in the tangential velocity gradient du/dy inside the boundary layer and the vortex sheet shrinking significantly, leading to the failure of the mathematical requirement of discontinuous tangential velocity; the presence of a small finite tangential velocity gradient is not strong enough to produce a vortex sheet. Hence, no vortex can be found.

Typically, the Prandtl-Meyer expansion fan will not intrude into the shock tube, or the expansion will stay outside the tube exit. As the rarefaction level increases, the expansion region at the tube exit does intrude into the tube's interior, but no diffracted wave is visible in the flow pattern in the transition regime.

V. CONCLUSIONS

In this work, attention has been primarily paid to the vortex loop formation caused by shock wave diffraction over a rectangular corner in dilute gas flows. Transient DSMC and compressible CFD simulations has been performed, and comparisons have been made between the results from the *dsmcFoamPlus* and *hy2Foam* where the Knudsen number allowed.

An increase in flow rarefaction results in the inner-structure of vortex loops becoming simpler and the flow patterns in all the simulations of this work are laminar. Thicker primary and embedded shock waves due to flow rarefaction have successfully captured by *dsmcFoamPlus*.

With the use of the rorticity, the rotational and shear movements of the fluid element can be effectively resolved. The circulation can be decomposed into a rorticity flux that describes the fluid-rotational strength of a vortex and a shear vector flux that represents the shear strength of a vortex. An isolated rorticity loop forms

within the vortex atmosphere described by streamlines. The rorticity flux of the isolated rorticity loop increases with the shock Mach number non-linearly and decreases with increasing Knudsen number. The increase of rorticity flux in the isolated rorticity loop with time is attributed to the transformation from the shear vector to rorticity. In the rarefied condition, there is a maximum Knudsen number limiting the generation of a vortex. The increase of the Knudsen number will thicken the Knudsen layer and the lateral vortex sheet, causing the failure in the condition of discontinuous tangential velocity. When the flow Knudsen number exceeds this maximum in the transition regime, no vortex loop forms. The vortex loops in the near continuum flow regime and the slip flow regime still have considerable ability to propagate forward. The radial size of the vortex loop increases with both the shock Mach number and the Knudsen number.

Further investigation can be conducted to explore the relationship between the vortex formation and the Knudsen number. Simulations with a more realistic nozzle geometry, vortex loop propagation ability, and the geometry effect on the vortex loop development with the rarefaction effect could be studied.

VI. APPENDIXES

A. Transient DSMC simulations with *dsmcFoamPlus*

Obtaining time-averaged results for a steady-state flow in the DSMC method is standard, but in a transient case, it is necessary to perform the same simulation many times and average the results for each individual time interval. A boolean variable *steadyStateCase* is introduced in the *dsmcDynamicLoadBalancing* class and can be specified in *system/loadBalanceDict*. If *steadyStateCase* is set as *true*, the simulation is running in the steady-state mode and the previous time directories will be deleted as the simulation progresses, since in those cases only the data with the most samples and lowest scatter is desired. However, if *steadyStateCase* is set *false*, all the time directories written out are saved to disk in order to perform an ensemble average.

A Python script called "*dsmcFoamPlusTransientAverageLoadBalance*" has been developed to run the simulations multiple times and perform the ensemble averaging. It can be found at <https://github.com/Kevin-Cao-gla/TransientDSMC-and-Rortex-scripts>. This script must be located in the base directory of a simulation, along with a *loadBalanceRun* script, which has previously been described in Ref 51. This script will perform the first simulation, then copy the case to a newly-created directory called "*FirstCalculation*", then clean the case directory to start the next ensemble until the number of samples that is defined by "*nCalculations*" is reached. The results generated in each ensemble are then averaged and written to the "*FirstCalculation*" directory. In the current work, the

Table V: User defined part in the Python script.

```
#####BEGINNING OF USER DEFINE PART#####
#
caseName = "XXXXXX/" #slash must be kept
#
#the working directory path = "/home/XXXX/OpenFOAM/XXXX-2.4.0-MNF/run/"#slash must be kept
#the directory where new data computed by another computer is saved
externalDataPath = "/home/XXXX/OpenFOAM/XXXX-2.4.0-MNF/run/"#slash must be kept
#
# Important! number of calculations needed.
nCalculations = 0
#How many times it has been calculated?
nComplete = 0
#Is the calculation interrupted?
calcInterruption = False
#Just do superposition for two individual data?
externalNumComplete=0
#
#####END OF USER DEFINE PART#####
```

macroscopic properties of interest are pressure, velocity, and temperature, so only the results of these properties are ensemble-averaged.

The Python code that the user can alter is shown in Table V.

The script can also be used to start the simulation again in the case of a halted system and power-off when using a personal computer, job time limitation on an HPC, or simply when a user needs to increase the number of samples and continue the simulation. The number of completed ensembles is defined by *nComplete* in the script, and a boolean variable called *calcInterruption* is defined to check if the simulation has been interrupted. As an illustration, if it is desired to run the simulation 10 times, but it stopped in the middle of the eighth calculation, one could set *nCalculations* and *nComplete* as 3 and 7 respectively because the eighth was not completed and set *calcInterruption* as *True*.

If the user wants to use two PCs or the combination of PC and HPC to calculate one case in order to improve the speed of calculation, the variable *externalNumComplete* can be used. For instance, if the HPC finished a simulation 20 times, which is considered as external data, and the PC finished it 40 times, and the data from both has already been ensemble-averaged separately, then *nComplete* can be defined as 40 and *externalNumComplete* as 20. The script will merge both results and average them. It is worth mentioning that when *externalNumComplete* is non-zero, the number in *nCalculations* will not work because the script is working in data-merging mode. Also, the *externalDataPath* should be set to the relevant case directory.

B. Rorticity calculator

Two methods to calculate the rorticity are given in [47] and [21]. The first uses the Newton iteration method⁴⁷ and the second is based on Schur decomposition²¹. The detail of definition, derivation and calculation procedures of rorticity is given in Ref. 47 and is not repeated here.

The calculation of rorticity in this work is based on the real Schur decomposition because of the method's high efficiency. Schur decomposition is already included in the *scipy* module in Python. The calculator used here reads the data or result files created through user-defined post-processing utilities or executable commands and then finds the rotational part in the domain. These utilities are rewritten by means of the vorticity utility in *OpenFOAM/applications/utilities/postProcessing/velocityField/vorticity* to read the velocity data *UMean* of each computational cell from a *dsmcFoamPlus* simulation and to calculate the corresponding velocity gradient tensor and vorticity vector. Interpolation schemes for *gradSchemes* in the *system/fvSchemes* file of each case must be declared before typing any executable commands. In this work, the second-order central difference scheme *Gauss linear* is used.

The order of the velocity gradient tensor is:

$$\frac{\partial u}{\partial x}, \frac{\partial v}{\partial x}, \frac{\partial w}{\partial x}, \frac{\partial u}{\partial y}, \frac{\partial v}{\partial y}, \frac{\partial w}{\partial y}, \frac{\partial u}{\partial z}, \frac{\partial v}{\partial z}, \frac{\partial w}{\partial z}$$

VII. DATA AVAILABILITY

The data that support the findings of this study are openly available from the University of Glasgow at <http://doi.org/10.5525/gla.researchdata.1136>.

REFERENCES

- ¹E. K. Ahangar, M. B. Ayani, and J. A. Esfahani. Simulation of rarefied gas flow in a microchannel with backward facing step by two relaxation times using Lattice Boltzmann method–slip and transient flow regimes. *International Journal of Mechanical Sciences*, 157:802–815, 2019.
- ²D. G. Akhmetov. *Vortex rings*. Springer Science & Business Media, 2009.
- ³G. A. Bird and J.M. Brady. *Molecular gas dynamics and the direct simulation of gas flows*, volume 42. Clarendon press Oxford, 1994.
- ⁴M. Brouillette and C. Hebert. Propagation and interaction of shock-generated vortices. *Fluid dynamics research*, 21(3):159–169, 1997.
- ⁵V. Casseau. *An open-source CFD solver for planetary entry*. PhD thesis, University of Strathclyde, 2017.
- ⁶S. Cooppan and B. Skews. Three-dimensional shock wave diffraction off a discontinuous edge. *Shock Waves*, 27(2):131–142, 2017.
- ⁷M. Darbandi and E. Roohi. A hybrid DSMC/Navier–Stokes frame to solve mixed rarefied/nonrarefied hypersonic flows over nano-plate and micro-cylinder. *International Journal for Numerical Methods in Fluids*, 72(9):937–966, 2013.
- ⁸T. R. Deschenes and J. Grot. Prediction of rarefied micro-nozzle flows using the SPARTA library. In *AIP Conference Proceedings*, volume 1786, page 080002. AIP Publishing LLC, 2016.
- ⁹Y.S. Gao and Liu C.Q. Rortex and comparison with eigenvalue-based vortex identification criteria. *Physics of Fluids*, 30(8):085107, 2018.
- ¹⁰A. Gavasane, A. Agrawal, and U. Bhandarkar. Study of rarefied gas flows in backward facing micro-step using Direct Simulation Monte Carlo. *Vacuum*, 155:249–259, 2018.
- ¹¹F. Gnani, K. H. Lo, H. Zare-Behtash, and K. Kontis. Shock wave diffraction phenomena around slotted splitters. *Aerospace*, 2(1):1–16, 2015.
- ¹²F. Gnani, K. H. Lo, H. Zare-Behtash, and K. Kontis. Shock wave diffraction in the presence of a supersonic co-flow jet. *Shock Waves*, 26(3):253–262, 2016.
- ¹³B. Goshayeshi, E. Roohi, and S. Stefanov. Dsmc simulation of hypersonic flows using an improved sbt-tas technique. *Journal of Computational Physics*, 303:28–44, 2015.
- ¹⁴B. Goshayeshi, E. Roohi, and S. Stefanov. A novel simplified bernoulli trials collision scheme in the direct simulation monte carlo with intelligence over particle distances. *Physics of Fluids*, 27(10):107104, 2015.
- ¹⁵S. Green. *Fluid vortices*, volume 30. Springer Science & Business Media, 2012.
- ¹⁶R. Groll. Micro diffuser flow modeling for cold gas propulsion systems. *PAMM*, 14(1):633–640, 2014.
- ¹⁷N. G. Hadjiconstantinou, A. L. Garcia, M. Z. Bazant, and G. He. Statistical error in particle simulations of hydrodynamic phenomena. *Journal of computational physics*, 187(1):274–297, 2003.
- ¹⁸X.Y. He, B.J. He, and G.B. Cai. Simulation of rocket plume and lunar dust using DSMC method. *Acta Astronautica*, 70:100–111, 2012.
- ¹⁹K. Kontis, R. An, and J. A. Edwards. Compressible vortex-ring interaction studies with a number of generic body configurations. *AIAA journal*, 44(12):2962–2978, 2006.
- ²⁰F. La Torre, S. Kenjereš, J-L Moerel, and C.R. Kleijn. Hybrid simulations of rarefied supersonic gas flows in micro-nozzles. *Computers & fluids*, 49(1):312–322, 2011.
- ²¹C.Q. Liu, Y.S. Gao, S.L. Tian, and X.R. Dong. Rortex—a new vortex vector definition and vorticity tensor and vector decompositions. *Physics of Fluids*, 30(3):035103, 2018.
- ²²M. Macdonald and V. Badescu. *The international handbook of space technology*. Springer, 2014.
- ²³H.X. Mao, D.B Fu, and X.D. Bao. Engineering method of predicting rocket exhaust plumes at middle and low altitudes. *Journal of Spacecraft and Rockets*, 54(5):1170–1177, 2017.
- ²⁴R. Mariani and K. Kontis. Effects of exit nozzle diameter on compressible vortex rings flow structure. In *47th AIAA Aerospace Sciences Meeting Including The New Horizons Forum and Aerospace Exposition*, page 410, 2009.
- ²⁵J. Martinez and E. Worthy. International Space Station (ISS) Thruster Plume Contamination and Erosion Control for Visiting Spacecraft. *Microscopy and Microanalysis*, pages 1–3.
- ²⁶S. Mazouffre, V. Caubet-Hilloutou, J.C. Lengrand, and E. Pawelec. Examination of the shock wave regular reflexion phenomenon in a rarefied supersonic plasma flow. *Physics of plasmas*, 12(1):012323, 2005.
- ²⁷P. H. Oosthuizen and W. E. Carscallen. *Introduction to compressible fluid flow*. CRC press, 2013.
- ²⁸M. Orlandi, A. Passaro, and R. Rampini. Need for a tool for the preliminary analysis of bipropellant plume impingement effects on contamination sensitive surfaces. In *Systems Contamination: Prediction, Control, and Performance 2016*, volume 9952, page 995209. International Society for Optics and Photonics, 2016.
- ²⁹R.T. Paton, B.W. Skews, and A. Saligram. Visualisation of plane shock wave diffraction from the curved exit of a shock tube. *Journal of Visualization*, 18(3):493–499, 2015.
- ³⁰F. Pellicani. Atmosphere Re-Entry Simulation Using Direct Simulation Monte Carlo (DSMC) Method. 2016.
- ³¹J. J. Peña Fernández and J. Sesterhenn. Compressible starting jet: pinch-off and vortex ring–trailing jet interaction. *Journal of Fluid Mechanics*, 817:560–589, 2017.
- ³²L. Qin, Y. Xiang, H.Y. Lin, and H. Liu. Formation and dynamics of compressible vortex rings generated by a shock tube. *Experiments in Fluids*, 61(3):1–16, 2020.
- ³³R. Ranjan, S.K. Chou, F. Riaz, and K. Karthikeyan. Cold gas micro propulsion development for satellite application. *Energy Procedia*, 143:754–761, 2017.
- ³⁴E. Roohi, S. Stefanov, A. Shoja-Sani, and H. Ejraei. A generalized form of the bernoulli trial collision scheme in dsmc: Derivation and evaluation. *Journal of Computational Physics*, 354:476–492, 2018.
- ³⁵P. G. Saffman. *Vortex dynamics*. Cambridge university press, 1992.
- ³⁶S. S. Sawant, O. Tumuklu, R. Jambunathan, and D. A. Levin. Application of adaptively refined unstructured grids in DSMC to shock wave simulations. *Computers & Fluids*, 170:197–212, 2018.
- ³⁷T. E. Schwartzentruber and I. D. Boyd. A hybrid particle-continuum method applied to shock waves. *Journal of Computational Physics*, 215(2):402–416, 2006.
- ³⁸K. Shariff and A. Leonard. Vortex rings. *Annual Review of Fluid Mechanics*, 24(1):235–279, 1992.
- ³⁹A. Shoja-Sani, E. Roohi, and M. Kahrom. Investigation of rarefied gas flow around naca 0012 airfoil using dsmc and ns solvers. In *Ankara International Aerospace Conference*, 2013.
- ⁴⁰A. Shoja-Sani, E. Roohi, and S. Stefanov. Evaluation of the generalized bernoulli trial-transient adaptive subcell (gbt-tas) collision scheme in treating rarefied gas flows. *Computers & Fluids*, 213:104740, 2020.
- ⁴¹A. Shoja-Sani, E. Roohi, and S. Stefanov. Homogeneous relaxation and shock wave problems: Assessment of the simplified and generalized bernoulli trial collision schemes. *Physics of Fluids*, 33(3):032004, 2021.
- ⁴²C. Shu, X.H. Mao, and Y.T. Chew. Particle number per cell and scaling factor effect on accuracy of DSMC simulation of micro flows. *International Journal of Numerical Methods for Heat & Fluid Flow*, 2005.
- ⁴³B. Skews, C. Law, A. Muritala, and S. Bode. Shear layer behavior resulting from shock wave diffraction. *Experiments in fluids*, 52(2):417–424, 2012.
- ⁴⁴B.W. Skews and J.J. Bentley. Merging of two independent diffracting shock waves. *Shock Waves*, 26(3):327–331, 2016.
- ⁴⁵S. Stefanov. On dsmc calculations of rarefied gas flows with small number of particles in cells. *SIAM J. Scientific Computing*, 33:677–702, 01 2011.

- ⁴⁶M. Sun and K. Takayama. Vorticity production in shock diffraction. *Journal of Fluid Mechanics*, 478:237–256, 2003.
- ⁴⁷S.L. Tian, Y.S. Gao, X.R. Dong, and .Q. Liu. Definitions of vortex vector and vortex. *Journal of Fluid Mechanics*, 849:312–339, 2018.
- ⁴⁸A. R. Tummala and A. Dutta. An overview of cube-satellite propulsion technologies and trends. *Aerospace*, 4(4):58, 2017.
- ⁴⁹D.S. Watvisave, B.P. Puranik, and U.V. Bhandarkar. Modeling wall effects in a micro-scale shock tube using hybrid MD–DSMC algorithm. *Shock Waves*, 26(4):477–489, 2016.
- ⁵⁰M. D. Weinberg. Direct Simulation Monte Carlo for astrophysical flows—I. Motivation and methodology. *Monthly Notices of the Royal Astronomical Society*, 438(4):2995–3006, 2014.
- ⁵¹C. White, M. K. Borg, T. J. Scanlon, S. M. Longshaw, B. John, D.R. Emerson, and J. M. Reese. dsmcFoam+: An OpenFOAM based direct simulation Monte Carlo solver. *Computer Physics Communications*, 224:22–43, 2018.
- ⁵²X.W. Xue, S. Chen, and Q.H. Sun. Investigation of shock attenuation in a shock tube using DSMC method. In *AIP Conference Proceedings*, volume 2132, page 070012. AIP Publishing LLC, 2019.
- ⁵³H.H. Zhang, Z.H. Chen, B.H. Li, and X.H. Jiang. The secondary vortex rings of a supersonic underexpanded circular jet with low pressure ratio. *European Journal of Mechanics-B/Fluids*, 46:172–180, 2014.